ELASTIC PION SCATTERING AT 50 MeV ON ^{40}Ca AND ^{48}Ca.

by

FRANCIS MARTIN ROZON

B.Eng.(Phys.), The University of Saskatchewan, 1983

A THESIS SUBMITTED IN PARTIAL FULFILLMENT OF THE REQUIREMENTS FOR THE DEGREE OF MASTER OF SCIENCE

in

THE FACULTY OF GRADUATE STUDIES

Department of Physics

We accept this thesis as conforming to the required standard

THE UNIVERSITY OF BRITISH COLUMBIA

October 1985

In presenting this thesis in partial fulfilment of the requirements for an advanced degree at the University of British Columbia, I agree that the Library shall make it freely available for reference and study. I further agree that permission for extensive copying of this thesis for scholarly purposes may be granted by the head of my department or by his or her representatives. It is understood that copying or publication of this thesis for financial gain shall not be allowed without my written permission.

Department of PHYSICS

The University of British Columbia
1956 Main Mall
Vancouver, Canada
V6T 1Y3

Date Oct. 20, 1985

Abstract

Absolute differential cross-sections have been measured for elastic $\pi^{\pm}$ scattering on ^{12}C, ^{40}Ca, and ^{48}Ca using the QQD Spectrometer. The ^{12}C data are in good agreement with (Sob 84a), indicating that the overall normalization of the data is good. The π^{+} ^{40}Ca data does not agree with the previously published data of (Pre 81) but fits the potential calculation using the SET E parameters (Car 82) better. Data for ^{48}Ca and π^{-} ^{40}Ca have not been previously published.

An optical potential model was used to describe the data. The potential parameters were fixed by fitting to the ^{40}Ca absolute cross-sections. The π^{-} differential cross-section ratios of the measured pair, (^{48}Ca, ^{40}Ca), were compared to calculations for which the ^{48}Ca neutron distribution had been fitted, either by varying the Fermi parameters, or by adding a truncated series of orthogonal polynomials to a starting Fermi form. Two forms of orthogonal polynomials were used; spherical Bessel functions as used in (Gyl 84, Bar 85)), and Laguerre polynomials as used in (Bar 85).

The rms radii differences obtained from the Fermi form fitting were found not to be independent of the optical potential used and to be sensitive to the inclusion of the ratio data in the diffractive region. Difficulties were encountered in obtaining reliable results from the orthogonal polynomial fits. The rms radii difference produced by the polynomial fits were not in agreement with results from the Fermi function fit. The neutron density distribution difference obtained from the polynomial fit is similar in form to the results of (Ray 81), but the

distribution peak is shifted toward the nuclear center. The rms radii differences found from the Fermi function and Fourier-Laguerre analysis are;

	Fermi	Fourier-Laguerre	
$\Delta_{nn'}$	.222 ± .048	.110 ± .022	(fm)

Table of Contents

Abstract.....ii
Table of Contents.....iv
List of Tables.....vi
List of Figures.....viii
Acknowledgements.....x

Chapter I INTRODUCTION 1
1.1 Measuring Nuclear Radii and Density Distributions.....5
1.1.1 Charge Probes.....6
1.1.2 Hadronic Probes.....7
1.1.3 Some Theoretical Approaches.....8

Chapter II THE EXPERIMENT 13
2.1 The M13 Beamline.....13
2.2 The QQD Spectrometer.....16
2.2.1 Detector Equipment.....16
2.2.2 Targets.....19
2.3 Data Aquisition Electronics.....20

Chapter III DATA REDUCTION 25
3.1 Cuts, Coefficients, and Angles.....25
3.1.1 Cuts in MOLLI.....26
3.1.2 Coefficients.....28
3.1.2.1 Front End Coefficients.....28
3.1.2.2 Spectrometer Coefficients.....29
3.1.3 Cuts in QQDANA.....32
3.1.4 The Spectrometer and Target Angles.....34
3.2 Peak Fitting.....35
3.3 Absolute Cross-Sections.....39
3.4 Cross-Section Ratios.....46

Chapter IV THE THEORY 48
4.1 Scattering Theory.....48
4.2 The Klein-Gordon Equation.....49
4.3 The Optical Potential.....50

Chapter V RESULTS 55
5.1 Absolute Cross-Section FIts.....58
5.2 Cross-Section Ratio Fitting.....64
5.2.1 Fermi Function Analysis.....64
5.2.2 Model Independent Analysis.....68
5.2.3 Discussion.....70

References.....77

List of Tables

Table 1.1 Some rms charge radii and nuclear radii differences from various experimental and theoretical methods. Errors are indicated where supplied by the references. All quantities are in fm.....11

Table 2.1 Target mass densities and scattering center densities of the experimental targets.....22

Table 3.1 Measured $\pi^{\pm}$ differential cross-sections for ^{12}C at 49.5 MeV.....43

Table 3.2 Measured $\pi^{\pm}$ differantial cross-sections for ^{40}Ca at 49.5 MeV.....44

Table 3.3 Measured $\pi^{\pm}$ differential cross-sections for ^{48}Ca at 49.7 MeV.....45

Table 3.5 $\pi^{\pm}$ diffential cross-section ratios for Calcium.....47

Table 4.1 The SET E optical potential parameters (Car 82).....54

Table 5.1 The Fermi distribution parameters used in this analysis. Note that for Krell code fitting, the charge distribution is set equal to the proton distribution. MIA refers to the Fermi parameter values used in the Fourier-Laguerre fits of section 5.2.2, while FIT B and FIT C refer to the best fit parameters from ratio fitting with those potentials to the whole angular range of the data set.....56

Table 5.2 The two best potential fits to the absolute ^{40}Ca differential cross-section angular distributions. The potential parameters that are not shown in the table remain at SET E values.....61

Table 5.3 The rms radii differences obtained by fitting Fermi density forms to the π^- ratio data for the "full" angular distribution and "reduced" set of angles as described in the text.....66

Table 5.4 The results of the Fourier-Laguerre (FL) model independent fits to the ratio data using the FIT C potential. The Fermi part of the density is described by the MIA parameters in Table 5.1.....71

List of Figures

Fig. 1.1 The $\pi^{\pm}p$ differential cross-sections at a) 160 MeV, and b) 50 MeV (from (Tac 84))....3

Fig. 1.2 The $\pi^{\pm}p$ total cross-sections (from (Tac 84))....4

Fig. 1.3 The density distribution difference produced by the model independent analysis of (Ray 81) (solid line) compared to results of a DME calculation of (Neg 72) (dashed line). The two solid lines represent the error bounds of the obtained density distribution difference....9

Fig. 2.1 The M13 Channel and QQD Spectrometer....14

Fig. 2.2 The QQD Spectrometer....17

Fig. 2.3 Target holder used for the Calcium targets. The nylon thread is shown as a dotted line between holes in the target frame and is anchored to the frame at the outermost holes....21

Fig. 2.4 The experimental electronic logic....24

Fig. 3.1 Typical Time-of-Flight (TOF) histogram for π^- in the M13 channel....27

Fig. 3.2 Showing a) the position of the ANGL cut, and b) the positions of the DDIF cuts....33

Fig. 3.3 Typical spectra for π^+ at 122 degrees for a) CH_2, and b) ^{48}Ca. ENAV is the average energy calculated from wire chambers 4 and 5....36

Fig. 3.4 Typical spectra for π^+ at 120 degrees for ^{48}Ca....38

Fig. 5.1 SET E calculations compared to the ^{40}Ca data; ● this experiment, ▲ from (Pre 81).....59

Fig. 5.2 FIT B (solid line) and FIT C (dashed line) potential fits to the ^{40}Ca data.....62

Fig. 5.3 FIT B (solid line) and FIT C (dashed line) potential fits to the ^{48}Ca data.....63

Fig. 5.4 The various Fermi function fits to the ratio data; FIT B full set (solid) and reduced set (dash-dot), FIT C full set (long dash) and reduced set (short dash). The fits are described in the text.....67

Fig. 5.5 The Fourier-Laguerre fits to the ratio data; three FL parameters (solid), five FL parameters (dashed).....72

Fig. 5.6 The density distribution difference produced by the Fourier-Lagurre fit (solid) compered to the proton analysis (dashed) of (Ray 81). The lines indicate the upper and lower error bounds obtained in the analyses.....73

Acknowledgements

The production of this thesis has been quite an extended effort. It turned out to be considerably longer than I had originally intentioned, but I was unable (unwilling) to significantly shorten it, while still preserving intact the bulk of what I wished to express (still, there has been much left unsaid, including at least five more pages of the possible misspellings of the word coffient... er, I mean, coefficient. I also had difficulties keeping my sentences short.

I would like to thank all those who have aided my thesis work in one way or another. Firstly, I have to thank my supervisor, Dick Johnson, for his efforts in trying to get me to finish this project, for sending me on a ski trip-conference to Lake Louise, and for instilling in me some of the enthusiasm for experimental physics that he demonstrates. Dave Gill has been a constant source of knowledge on the QQD spectrometer and M13 line. Hans Roser was invaluable in the preparation and running of the experiment itself, saving me many possible headaches.

Bruce Barnett, being the most senior graduate student in the group, has been greatly appreciated for his knowledge and for his sense of humour. His many helpful suggestions during the analysis, and guidance in the use and modification of several lengthy, incompletely documented programs has been invaluable. I would like to thank, en masse, all the other graduate students in the group, including Nigel Hessey, who misspelt my name in his thesis, and all others who contributed to the experiment.

TRIUMF also deserves mention for providing the facilities used in the experiment and analysis, as does NSERC, who funded my work. I would also like to thank Lori Murray. Her extensive patience and excellent backrubs have been greatly appreciated during the course of this work.

Chapter I

INTRODUCTION

The study of the structure of the atomic nucleus has been a topic of much interest for many decades now. In 1911, Rutherford (Rut 11) demonstrated by the scattering of alpha (α) particles that the atomic nucleus had to be smaller than 10^{-11} cm, several orders of magnitude smaller in size than the atom itself. The nature of the force that held or bound the nucleus together so tightly remained largely a mystery until Yukawa (Yuk 35) proposed the existence of a meson which would mediate the nuclear force much in the same way that the photon mediated the electromagnetic interaction. The meson's mass was then estimated to be about 200 times the electron mass, or ~ 100 MeV.

The meson was correctly identified in 1947 (Lat 47) as the pion. The pion proved to be an interesting particle, existing in three charge states, one state with a neutral charge and states with plus or minus one electronic unit of charge, all with a mass ~ 135 MeV, or about 270 times that of the electron. The pion-nucleon system proved to be a fruitful experimental ground, yielding several resonances, the most noticeable being the Δ_{33} resonance characterized by the quantum numbers of spin 3/2 and isospin 3/2. The Δ_{33} resonance is a wide (width Γ ~ 100 MeV) resonance which peaks at a laboratory kinetic energy of 195 MeV or a total center-of-mass energy of 1232 MeV. In particle property tables, it is denoted by its center-of-mass energy as the $\Delta(1232)$ to distinguish it from other resonances of the same quantum numbers.

In the energy region where the Δ_{33} resonance dominates, the pion-nucleon system demonstrates a large isospin sensitivity. If one considers the elastic scattering channels only for the moment, then decomposing the pion-proton system (the neutron can be treated in a symmetric manner) into the isospin states gives

$$| \pi^+ p > = | I = 3/2 >$$

$$| \pi^- p > = \sqrt{1/3} | I = 3/2 > + \sqrt{2/3} | I = 1/2 >.$$

If the isospin 1/2 channel is assumed to be negligible at the resonance, then the cross-section ratio (π^+p/π^-p), which is proportional to the square of the ratio of the matrix elements describing the elastic processes (or to the fourth power of the ratio of the decomposition coefficients), is expected to be 9. This treatment is justified by examining the 160 MeV cross-sections shown in Fig. 1.1a). If the single charge exchange channel is included, the ratio is expected to drop to 3, as shown in Fig. 1.2. At lower energies (~ 50 MeV) the resonance sensitivity is much weakened but Fig. 1.1b) demonstrates that there is still marked isospin preference in the interaction especially at back angles.

The pion-nucleus (bound nucleons) interaction is not the same as the free pion-nucleon interaction. Although one expects there to be relationships between the two processes, the isospin sensitivity may not necessarily carry over into the pion-nucleus system. Several theses by other students in the PISCAT group have demonstrated that the sensitivity is indeed still present in studies of elastic pion scattering (Gyl 84, Bar 85) and inelastic pion scattering (Tac 84, Sob 84a) on nuclei in the s-d shell region. This work attempts to extend these methods into the $f^{7/2}$, shell studying the two closed shell calcium

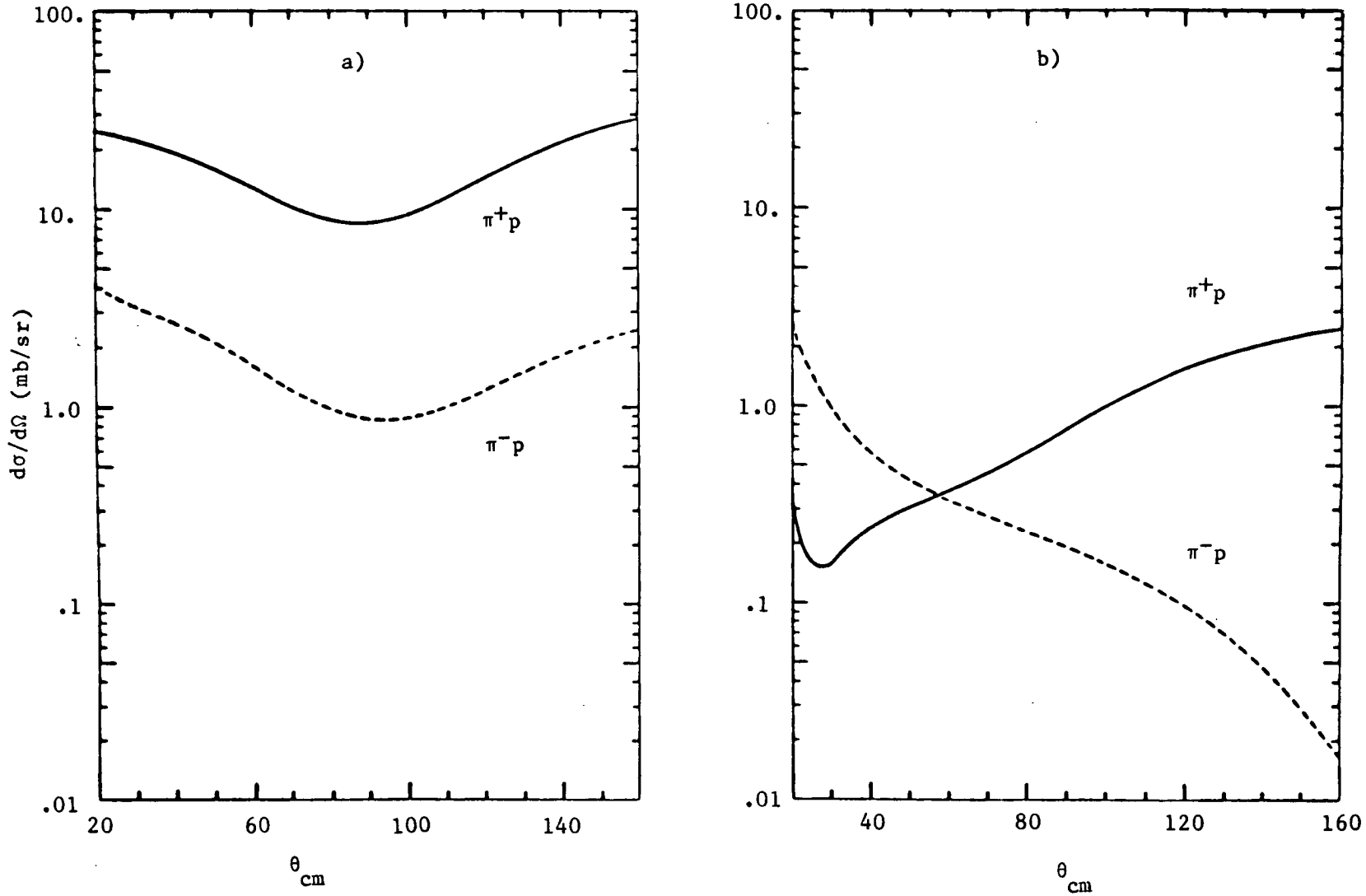

Fig. 1.1 The $\pi^{\pm}$ p differential cross-sections at a) 160 MeV, and b) 50 MeV (from (Tac 84))

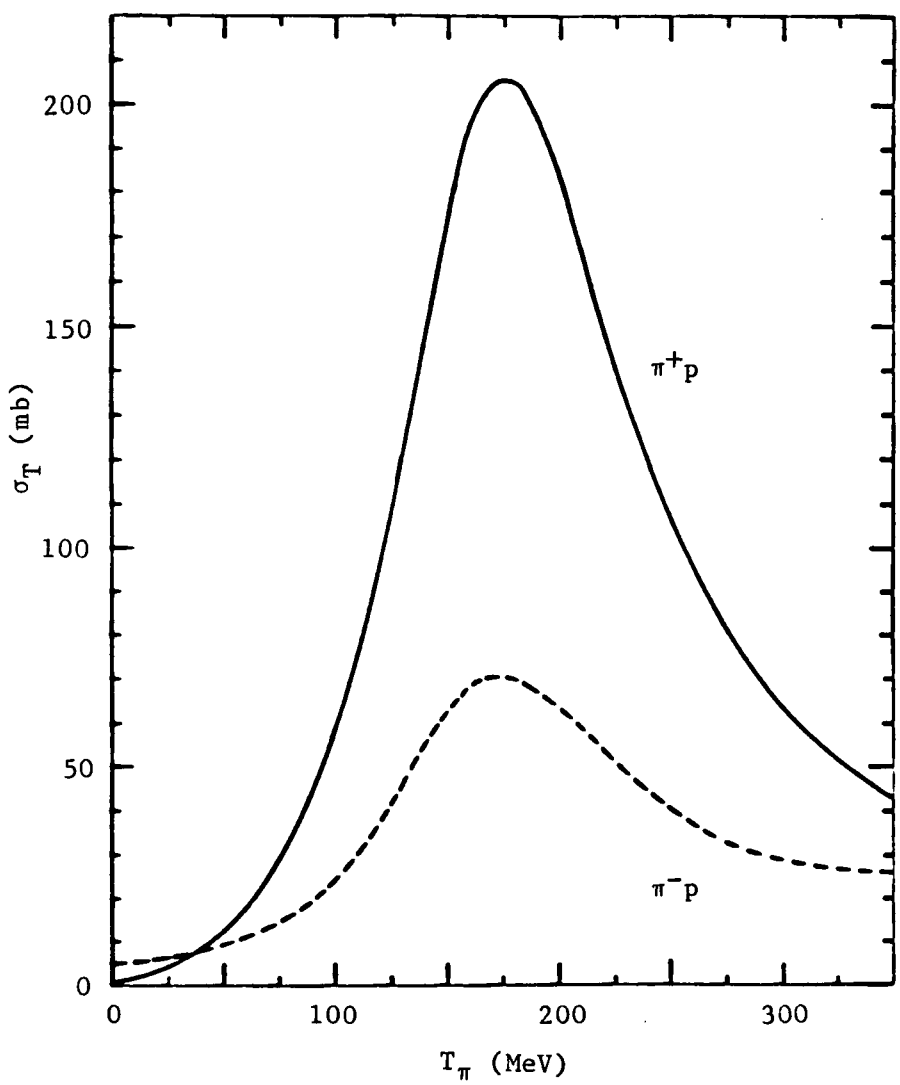

Fig. 1.2 The $\pi^{\pm}$ p total cross-sections
(from (Tac 84))

nuclei.

1.1 Measuring Nuclear Radii and Density Distributions

A property of the nucleus which can be measured with reasonable ease, though not completely unambiguously, is its size. The ambiguity arises from the fact that the nucleus is not a sharply defined sphere, but has a diffuse edge. As a result of the diffuse edge, the definition of the nuclear radius is somewhat difficult. A common measure of the radius is the root mean square (rms) radius defined by

$$\langle r^2 \rangle^{1/2} = \left[\frac{\int r^2 \rho(r)\, d^3r}{\int \rho(r)\, d^3r} \right]^{1/2}$$

where $\rho(r)$ is the nuclear density. The resulting rms radius is somewhat model dependent, that is, the derived rms radius depends to some extent upon the functional form chosen for the density.

The earliest definitive size determinations used α particle scattering and examined the cross-sections for deviations from the Rutherford (Coulomb) scattering law. A deviation implied that the probe had reached the interaction range of the strong force. From these early experiments, an empirical nuclear size law was established

$$r_{nuc} \sim A^{1/3}$$

where A denotes the atomic number of the nucleus.

With the development of various particle accelerators, the use of electron scattering to measure charge distributions to a high degree of accuracy became possible. Several exceptions to the $A^{1/3}$ rule soon appeared. For the two closed shell calcium isotopes, ^{40}Ca and ^{48}Ca, it was found (Fro 68) that the rms charge radius of ^{48}Ca was actually

smaller than that of ^{40}Ca.

For a reliable method of comparing various experimental and theoretical results several derived quantities are useful, namely

$$\Delta_{np} = \langle r^2_n \rangle^{1/2} - \langle r^2_p \rangle^{1/2}$$

$$\Delta_{nn'} = \langle r^2_n \rangle^{1/2}_A - \langle r^2_n \rangle^{1/2}_{A'}$$

and

$$\Delta_{pp'} = \langle r^2_p \rangle^{1/2}_A - \langle r^2_p \rangle^{1/2}_{A'}$$

conventionally defined such that $A' < A$, that is, the nucleus with less nucleons is denoted by the primes.

For the calcium isotopes under study here, various experiments show that

$$\langle r^2_n \rangle^{1/2}_{40} \simeq \langle r^2_p \rangle^{1/2}_{40} \simeq \langle r^2_p \rangle^{1/2}_{48}$$

so that essentially the neutron rms radius of ^{48}Ca is the only quantity to be determined.

1.1.1 Charge Probes

The lepton-nucleus interaction is taken to be the well known electromagnetic interaction. As there are then no ambiguities in the results arising from uncertainties in the interaction, one can concentrate upon the nuclear charge distribution parameters by themselves.

By about ten years ago or so, the sophistication of electron scattering data had reached the point where the data was of sufficient precision and covering a large enough region of momentum transfer that

model independent charge densities became necessary for good data fits (for example see (Fri 79)). These model independent densities took the form of sum-of-gaussian (SOG) or Fourier-Bessel (FB) expansions.

Another leptonic probe is the muon. Due to its large mass (~200 electron masses), the radius of the muonic orbit lies well inside the electron cloud and its wavefunction appreciably overlaps the nucleus. The muonic atom is then quite sensitive to the nuclear charge distribution. The so-called Barrett moments are obtained from the muonic atom data and combining them with the appropriate electron scattering data, one can obtain high precision model independent rms radii (see (Woh 81)).

The proton rms radii should be obtainable from the charge radius in a straightforward manner as the protons carry the bulk charge of the nucleus. However, allowance must be made for the proton and neutron charge form factors as well as a spin-orbit correction (Ber 72) in nuclei where there are unfilled ℓ-shells. The proton distribution can also be unfolded taking these effects into account, but the unfolding procedure can be rather cumbersome. To examine the neutron distribution, leptonic probes are not of much direct use, thus hadronic probes have to be used.

1.1.2 Hadronic Probes

Unlike the leptonic probes, hadronic probes are directly sensitive to the neutron distribution through the effects of the strong interaction. However, as there exists no convenient and exact description of the strong interaction as there is for the electromagnetic probe, an additional source of uncertainty is introduced into the problem. The pion's capabilities as a probe of the neutron density will be discussed more later in this work. The proton and the α particle have been

extensively used as nuclear probes and supply some experimental results for comparison to the pion data.

The proton is probably the most common hadronic probe due to its availability at high fluxes over wide energy regions. The energy region about 1 GeV kinetic energy has provided some of the best quality proton data for density determination. An optical potential of the Kerman, McManus, and Thaler (Ker 59) type is used in the cross-section calculation and some of the more recent analyses have extended the potential to second order (Ray 81, Cha 78, Var 77). The results of such analyses are usually in good agreement with theoretical models and data from other probes, but the agreement is not much improved, and often worsened, with the inclusion of these second order terms. The sophistication of these analyses has increased substantially over the past decade to the point where model independent methods are beneficial. The neutron density distribution difference obtained by (Ray 81), for the isptopes ^{48}Ca and ^{40}Ca, is shown in Fig. 1.3 along with results of a DME calculation (Neg-72) for comparison.

The α particle is conceptually a convenient probe as it has spin and isospin of zero. However, the α is strongly absorbed at all energies and thus is sensitive primarily to the nuclear surface. If experimental data is taken over a sufficiently large angular region, that is, into the rainbow scattering region, the α can probe the nuclear interior. A good example of this type of experiment and the associated analysis is given by (Gil 84) and references contained therein.

1.1.3 Some Theoretical Approaches

One of the major thrusts of theoretical nuclear structure

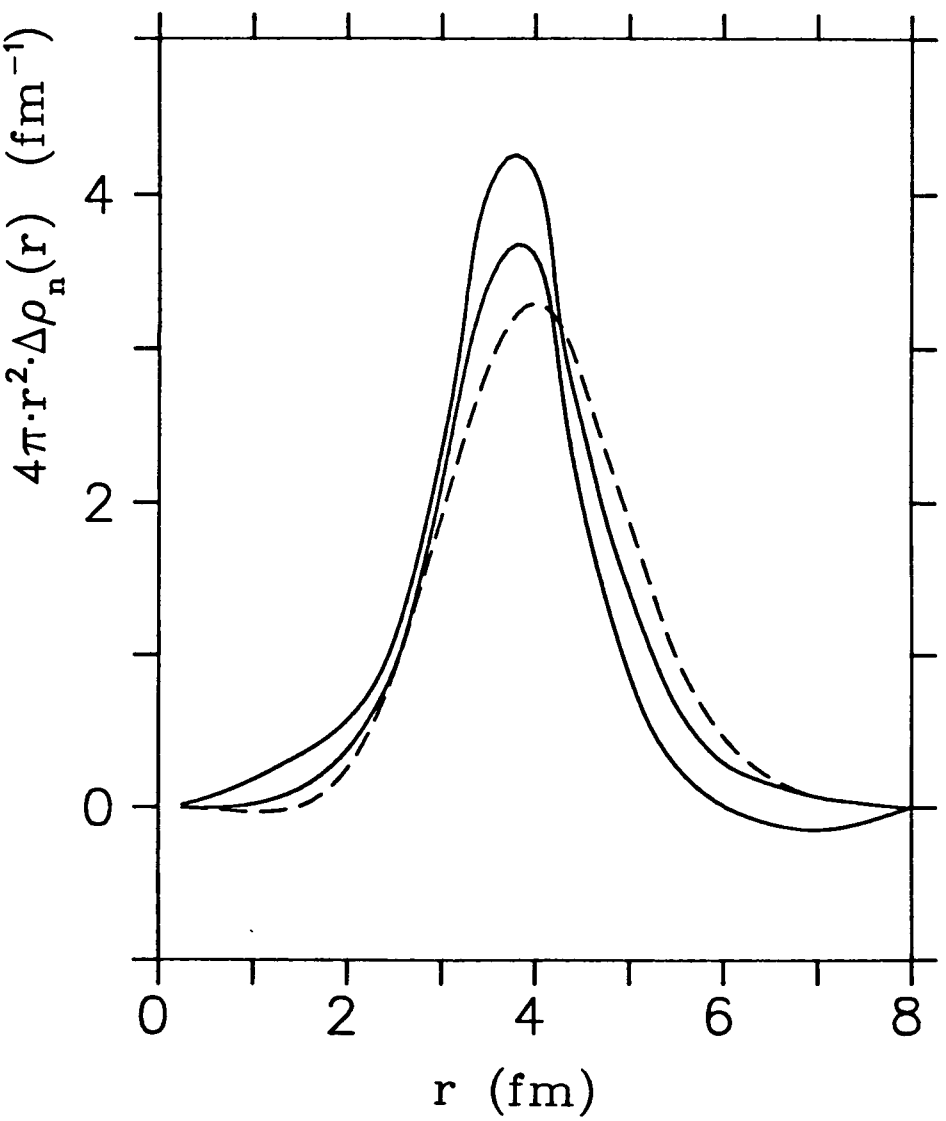

Fig. 1.3 The density distribution difference produced by the model independent analysis of (Ray 81) (solid line) compared to results of a DME calculation of (Neg 72) (dashed line). The two solid lines represent the error bounds of the obtained density distribution difference.

calculations of the 1960's and early 1970's was the adaptation and development of self-consistent field (SCF) approaches to nuclear physics. SCF methods were developed in several forms, some of the better models being the density-dependent Hartree-Fock (DDHF) of (Neg 70, Vau 70, Vau 72) or the density-matrix-expansion (DME) of (Neg 72). These theories provided a suitable framework for a variety of calculations but they were not without adjustable parameters. The parameters are fit to reproduce single particle energies, density distributions, and nuclear matter binding energies. The resulting densities agree reasonably well with selected data, and extracted quantities such as Δ_{np} and $\Delta_{nn'}$ were for the most part consistent with experimental results, but not for all models.

In addition to various SCF calculations, the use of the Coulomb energy difference of mirror pairs of nuclei could be used to find a value for Δ_{np}. This proved to be an unsatisfactory approach as unreasonable values of Δ_{np} were often required to explain the energy difference (Nolan-Schiffer anomaly (Nol 69)). The radii differences produced in this way were up to an order of magnitude different from experimental values for $A > 40$.

The shell model can also be used to predict the radii differences. However, results tended to overestimate Δ_{np} (Bat 69). More recent calculations have been done for the sulpher and magnesium isotopes (Gyl 84) which give good agreement but no similar results are available for the calcium isotopes.

A summary of some of the results for charge radii and nucleon radii differences obtained by various probes and theoretical approaches is given in Table 1.1. As the calcium nuclei have been widely studied, there

Method	Ref.	charge rms radius ^{40}Ca	charge rms radius ^{48}Ca	Δ_{np}^{40}	Δ_{np}^{48}	$\Delta_{nn'}$
e-	Fro-68	3.4869	3.4762			
μ^-	Woh-81	3.483(3)	3.482(3)			
p	Ray-81					.16(5)
	Ray-79			.10(5)	.23(5)	.13(4)
	Var-77			-.07	.21	.27
α	Gil-84			-.02(4)	.17(4)	.21(5)
DDHF	Neg-70			-.04	.23	.31
	Vau-72	3.49	3.54	-.05	.18	.18
π σ_T	Jak-77					.14(5)
π-atom	Pow-80			.001(34)	.207(65)	.229(44)

Table 1.1 : Some rms charge radii and nuclear radii differences from various experimental and theoretical methods. Errors are indicated where supplied by the references. All quantities in fm.

is a good data base for comparison to results from this experiment.

Chapter II

THE EXPERIMENT

This experiment was conducted during the summer of 1984 at the Tri-University Meson Facility (TRIUMF). The facility's cyclotron has several primary beam lines and can produce intense proton beams in the energy region of 180 MeV to 520 MeV. The meson hall's secondary beamlines feed off the primary beam line 1A. The pions used in this experiment are produced at the 1AT1 production target, a 10 mm pyrolytic graphic target, by a 500 MeV unpolarized proton beam, typically at a current of 130 μA.

2.1 The M13 Beamline

The pion beam line used in this experiment is the M13 (Ora 81) line. The M13 beam line is capable of handling up to 65 MeV pions, pions of higher energy not being copiously produced at the beam take-off angle of 135 degrees with respect to the primary beam. The beam line produces dispersed foci at F1 and F2 (see Fig. 2.1) and an achromatic focus at the scattering target location. The beam line transports protons, α's, muons and electrons in large quantities as well as pions. The heavier particles are ranged out by a CH_2 absorber placed before the second channel dipole so that they do not make it to the scattering target. The separation of the electrons and muons from the pions is done by time-of-flight down the channel.

The momentum spread of the incident pion beam is controlled by mechanical slits placed at F1. For a width of .5% Δp/p (or a 6 mm slit width), the π+ flux was ≈ 1.2 (10^6) per second. The F2 position

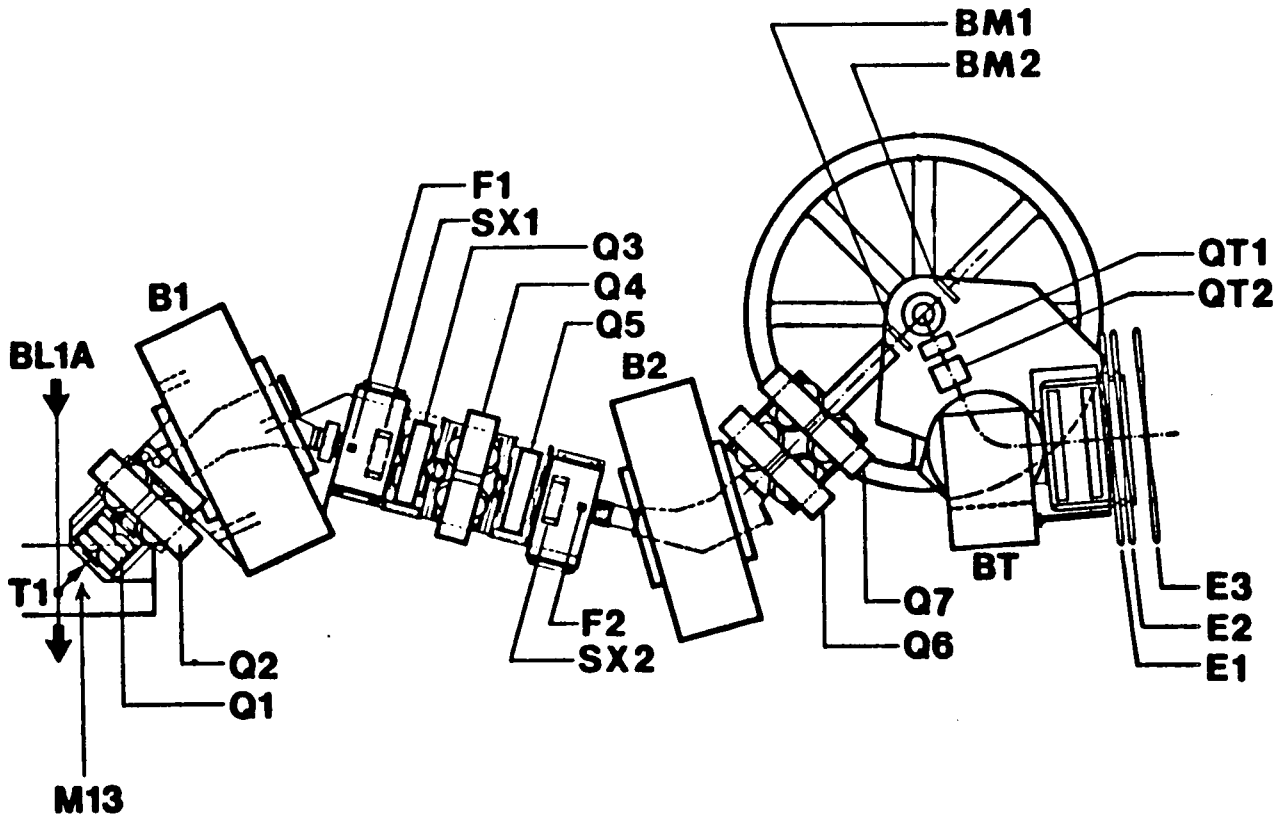

Fig. 2.1 The M13 Channel and QQD Spectrometer

contained a position sensitive (1/10 inch wire spacing), fast readout wire chamber to monitor the pion path in the channel and provided additional momentum information for the pions. The F2 chamber was only used for the π^- data. For the π^+ beam setting, the presence of large fluxes of protons and α's (other positively charged heavy ions are possibly also present) in the pion beam make the F2 counter inefficient. The F2 chamber allows one to use a wider channel acceptance for increased flux. For the π^- data, a 2% $\Delta p/p$ (25 mm F1 slit width) setting was used which provided a flux of $\simeq$ 1.1 (10^6) π^- per second.

The beam line magnet settings (as well as the spectrometer magnets) are controlled remotely by REMCON and the field strengths are monitored by hall probes in the quadrupoles and NMR probes in the dipoles. The probes are useful in reproducing beam tunes and also in monitoring magnet stability. The channel sextupoles were not used in this experiment. The purpose of the sextupoles is to straighten the focal plane at F2 for better momentum definition, but their usefulness has not yet been reliably demonstrated.

The pion beam flux is monitored by three different pairs of plastic scintillators (NE110) which have been fitted with RC8575R phototubes. The primary beam flux monitoring pair are the BM1 and BM2 scintillators. BM1 is a thin scintillator (.8 mm) and is placed before the scattering target, while BM2 is downstream of the target and is 6.4 mm thick. The coincidence BM1•BM2 is a measure of the absolute flux. The remaining two pairs of counters are called muon counters as they count muons produced by pions decaying in the channel. Each pair of counters is oriented at 7 degrees to the beam line. The coincidences μ1•μ2 and μ3•μ4 are then used as relative beam flux monitors and are especially useful at very forward

angles where the spectrometer blocks the flux before it reaches BM2. The ion chamber and Cerenkov counter around the T1 production target can also be used as relative flux monitors.

2.2 The QQD Spectrometer

The QQD (quadrupole-quadrupole-dipole) spectrometer (Sob 84b) was used to measure the momentum of the scattered pions. The quadrupoles QT1 and QT2 serve to give the spectrometer a large solid angle (~16 msr) and the dipole BT bends the scattered pions 70 degrees horizontally to the left for eventual dispersion matching. The focal plane of the spectrometer is beyond the last wire chamber and tilted at 72 degrees to the central ray of the spectrometer. The spectrometer is shown in Fig. 2.2.

During this experiment only QT2, the vertically focussing element, was used. When the first quadrupole, which is horizontally focussing, is in use, it should provide approximately a 5-10% increase in solid angle but will likely reduce the reliability of the target traceback which is found using no delta dependence. The solid angle improvement has not been very well established however, so that QT1 is not regularly used.

2.2.1 Detector Equipment

The pion trajectory is monitored by four Multi Wire Proportional Counters (MWPCs) or Wire Chambers. Two chambers are positioned before the spectrometer dipole on opposite sides of QT2 at the WC1 and WC3 locations. The remaining two chambers are placed after the dipole. The chambers are constructed with three parallel planes of equally spaced wires. The middle or anode plane is supplied with a positive high voltage

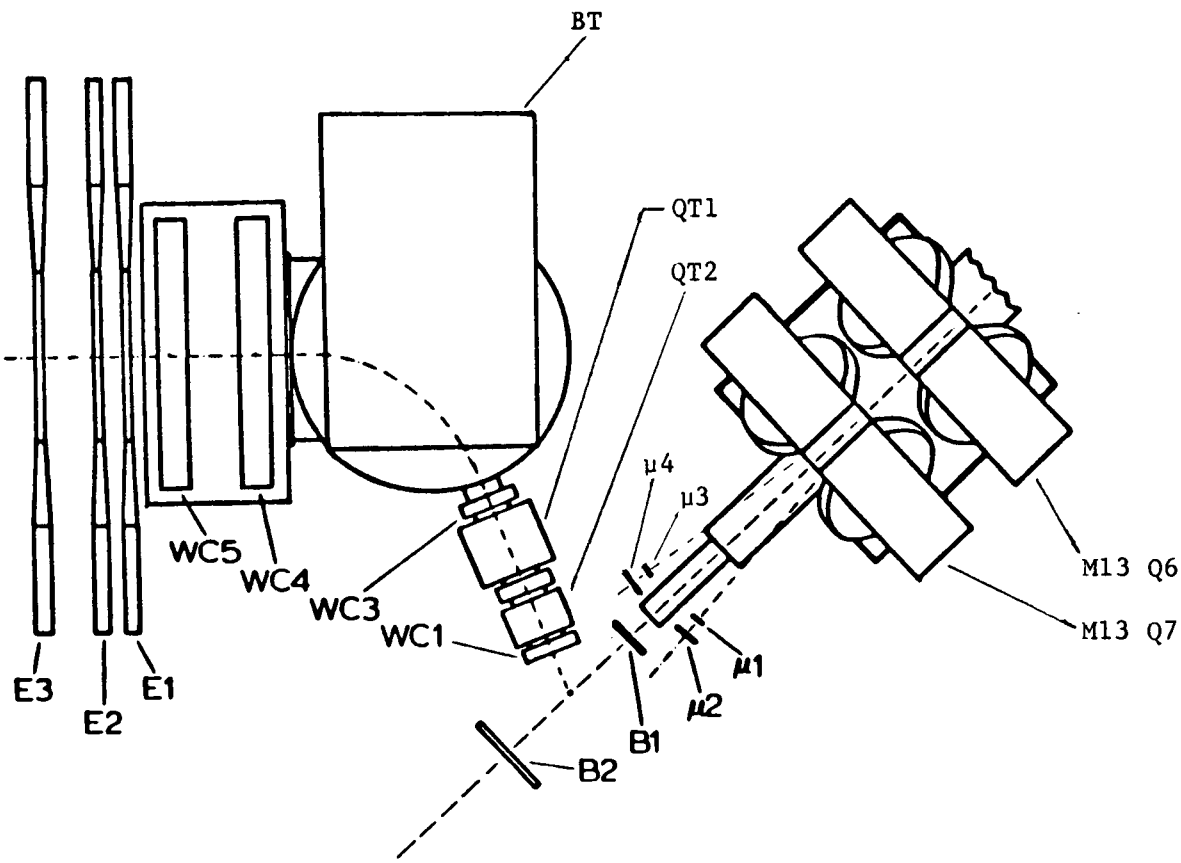

Fig. 2.2 The QQD Spectrometer

while the outer cathode planes are grounded. The wires of one cathode plane are oriented parallel (horizontally) to the anode wires and provide y-direction information. The other cathode plane is oriented perpendicular to the anode wires and provide x-direction information. The cathode wires connect to printed circuit delay lines. Both ends of the delay line are timed with time-to-digital convertors (TDC's) and the difference of the times provides a measure of the particle position in the chamber. Further details concerning the construction and operation of the counters are provided in (Tac 84, Hes 85).

The method of construction of the wire chambers provides a convenient approach to their calibration. What is needed is a conversion factor to convert the TDC differences to a position in millimeters and an offset to define the chamber center. That is,

$$X_i = m_i \cdot t_i + b_i$$

where X, m, t, and b are respectively the position, the conversion factor, the TDC difference value and offset in the i^{th} coordinate. The offset is set such that, in the TDC difference spectrum, the beam spot edges appear at $\pm X^\circ/2$, X° being the beam size in that particular chamber which is assumed (for those coordinates that are defined only by one wire chamber segment as is the case for all coordinates but WC4X and WC5X) to be symmetric. The conversion factors for the y-planes are found by examining the "picket fence" structure that is obtained in the y TDC difference data. The y-direction cathode plane wires are parallel to the anode wires. When ionized electrons avalanche around an anode wire, a strong pulse will be created in that anode wire and through capacitive coupling, in the nearby cathode wires. The x-plane can see a smooth

spectra of avalanche locations, but the y-plane sees quantized positions corresponding to the individual anode wires. As the anode wires are 2 mm apart, one can obtain from the separation in the TDC spectra peaks a conversion factor to distance.

The two backend chambers are divided horizontally into three segments of 203 mm size (Tac 84). A particle passing between the edges of the segments is likely to fire both segments, thus if one looks at the positions in the central segment of the double hits with the left or right segment that occur, one can obtain both the necessary calibration factor and offset for the central segment to put the double hits peaks at ± 101.5 mm. The left and right segments are taken to have the same calibration factor as the middle segment and the offset is adjusted to match the central segment edge. The front end chambers are single segment only, so the chamber edge can not be as conveniently defined. The conversion factor is then taken equal to the y value. This is reasonable to assume as the x- and y-planes are constructed in a symmetric manner and are read by the same TDC.

The spectrometer also has three scintillators placed after the last wire chamber. These scintillators form part of the event definition as will be discussed below. The scintillators are large enough to cover most of the back end wire chambers. E1 and E2 are 6.4 mm thick and E3 is 12.8 mm. Three scintillators are used to help reduce the background and random events.

2.2.2 Targets

Three targets were used in this experiment; CH_2, ^{40}Ca and ^{48}Ca targets. The CH^2 target is in the form of a plastic plate which can be

easily cut to fit the spectrometer target ladder. The CH_2 target is large enough such that all of the pion beam intercepts the target. The ^{40}Ca target was made of two self supporting plates of metallic natural calcium (97% ^{40}Ca) of size 51 mm by 39 mm held in a target holder of the design indicated in Fig. 2.3 by thin nylon thread. The target holder is of dimension such that it does not intercept any of the beam at the angles measured in the experiment. The nylon thread is small enough so that its background contribution is not significant. In this manner the necessity to measure an "empty" target is eliminated. The ^{48}Ca target is an isotopically enriched, self supporting metallic plate 31.8 mm by 16.1 mm on loan from Los Alamos and was mounted in a target holder in a similar manner to the ^{40}Ca target.

Calcium oxidizes rapidly in air so it must be keep in a neutral environment during the experiment so that the target mass does not change during the run. For this purpose, the target chamber was filled with argon and helium when the targets were being mounted on the target ladder and it was evacuated during the running. The ^{40}Ca target was cleaned in a neutral atmosphere and weighed before the running period and again after the run. Due to the expensive nature of the ^{48}Ca target, it was not cleaned and was heavily contaminated with what is believed to be primarily oxygen. The ^{48}Ca target was also weighed twice. The target mass densities are given in Table 2.1 along with the density of scattering centers.

2.3 Data Acquisition Electronics

For this experiment, the electronic equipment used is basically the standard QQD setup as described in previous group theses (Bar 85, Gyl 84,

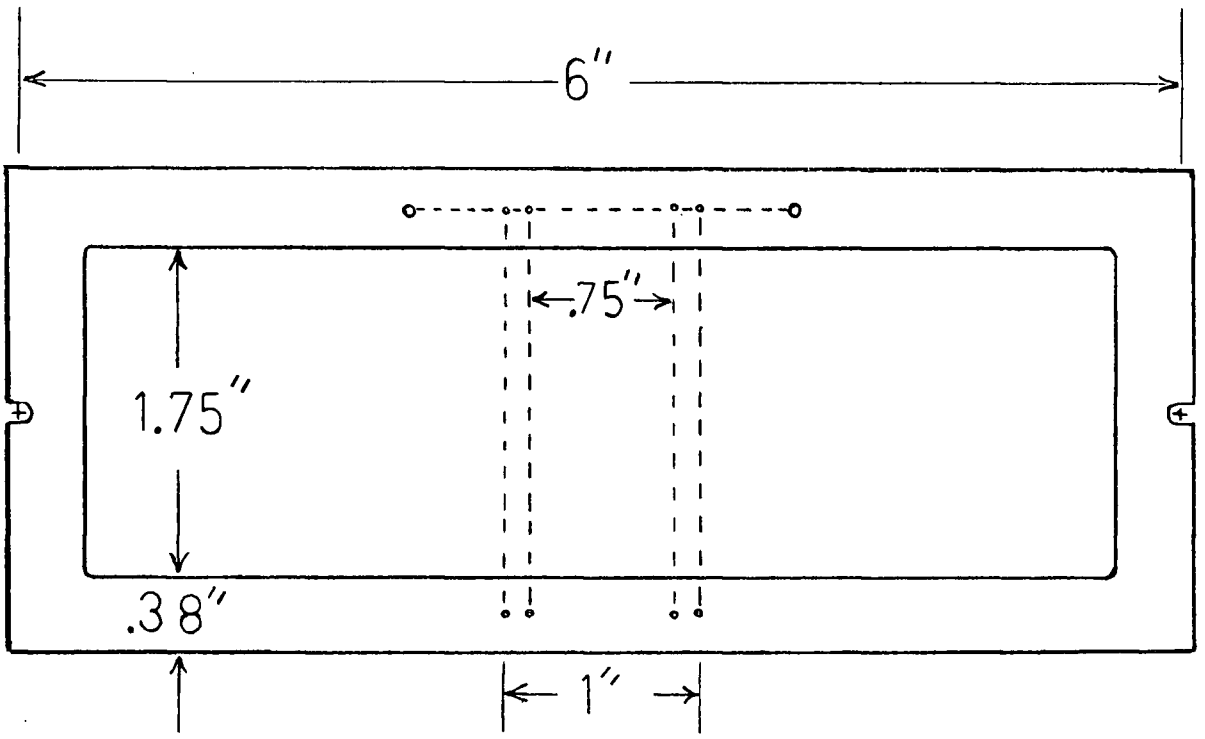

Fig. 2.3 Target holder used for the Calcium targets. The nylon thread is shown as a dotted line between holes in the target frame and is anchored to the frame at the outermost holes.

Target	Nucleus	Mass Density (mg/cm^2)	N_{tgt} (cm^{-2})
CH_2	^{12}C	137	6.87×10^{21}
	^{1}H	23.0	1.38×10^{22}
^{40}Ca	^{40}Ca	288	4.33×10^{21}
^{48}Ca	^{48}Ca	99.9	1.25×10^{21}
	^{16}O	12.1	4.55×10^{20}

Table 2.1 Target mass densities and scattering center densities of the experimental targets.

Sob 84a, Tac 84) with a few minor additions primarily to accomodate the F2 counter and the added moun counters, μ3 and μ4. The spectrometer data was recorded on magnetic tape for later off-line analysis and was also analyzed to some extent on-line. The TRIUMF standard data acquisition program DA, run on a PDP-11/34 computer using the RSX operating system, collected the spectrometer data which was in the form of TDC, ADC (analog-to-digital convertor) and scaler values plus bit patterns from the C212 and MALU (for the F2 chamber readout) units. The on-line analysis was done with a modified version of MULTI.

The program DA responds to LAM's (look-at-me's) generated in a specific CAMAC module. The LAM's are produced by spectrometer events or beam samples. The electronic logic is shown in Fig. 2.4. A spectrometer event is defined as the coincidence BM1•E1•E2•E3 with E1 defining the timing. The large scintillators E1, E2, and E3 had two or four phototubes each which were mean timed to make the event timing position independent. All spectrometer phototube signals were recorded in ADC's for energy information and some were recorded in TDC's for timing information.

A useful feature of the logic arrangement is that the gating used in the electronics serves to remove the necessity of applying dead-time corrections to the data by inhibiting all the electronics (including the scalers) while an event is being processed to tape. The F2X data is used as a software AND only. Data that has no F2X information is still recorded on tape, which includes all π^+ and ~ 25% of the π^- data. More detailed descriptions of the electronics can be found in the above mentioned theses.

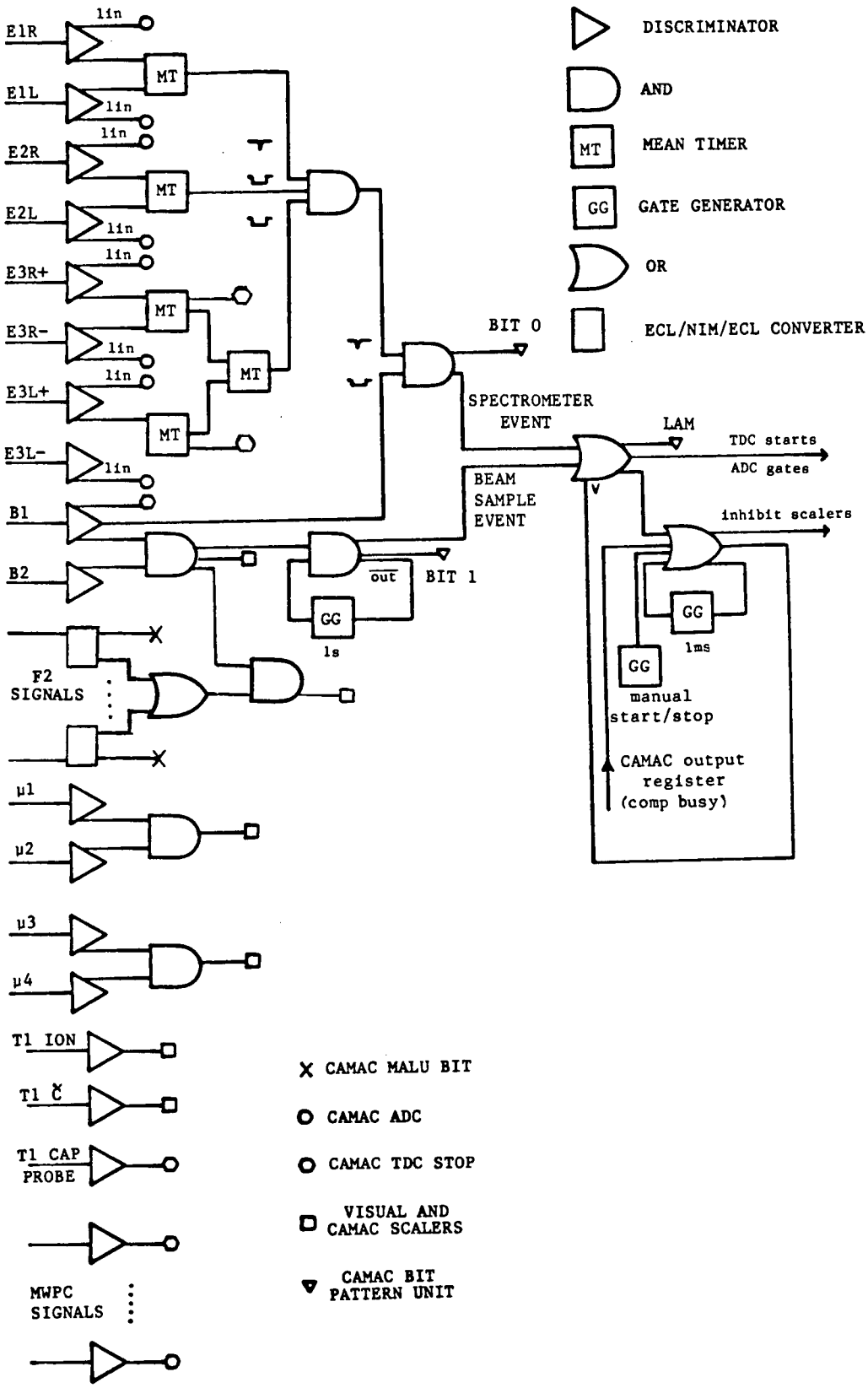

Fig. 2.4 The experimental electronic logic

Chapter III

DATA REDUCTION

In essence, the analysis consists of several stages; determining the number of elastically scattered pions from the given target material at each measured angle, applying various correction factors to the total number of pions to obtain the differential cross-section angular distributions, and fitting an optical model calculation to the angular distributions. The analysis up to the point of obtaining the cross-sections shall be discussed here. The optical model fitting is discussed in Chapter 5.

3.1 Cuts, Coefficients, and Angles

Two types of event data are written onto the magnetic tape by the on-line computer; spectrometer events defined by the coincidence BM1•E1•E2•E3, and beam sample events defined by BM1•BM2 taken about once per second. The coincidence definition of the spectrometer events reduces the random rate so that the magnetic tapes contain mainly good events and the data taking rate is reasonable (<100 events per second). The data defined by the BM1•BM2 coincidence is used to determine the beam fraction of pions, muons, and electrons that are detectable in the scintillators (discriminator thresholds may discard a lot of the electrons). For π^+ the pion beam fraction is determined to be 93%, and for π^- it is 91%. These fractions are obtained from the time-of-flight spectra (that is, time-of-flight of the particles down the beam line), an

example of which is shown in Fig. 3.1.

3.1.1 Cuts in MOLLI

The program MOLLI is used to process the data to the point where it is ready for pion momenta calculations. Various cuts on the data are applied in MOLLI; only spectrometer events are considered, all wire chamber TDC's must contain "real" data (that is, no zeroes or full scales), the sums of the TDC values from each end of the delay line must lie within specified limits, and in the back two wire chambers, the left and right segments must not fire for the same event. These cuts then ensure that reliable position data exists in the x and y coordinates for each wire chamber. The sum cut is useful when a chamber functions poorly with a lot of noise, creating improper position readings or when it experiences multiple pion hits. WC3 experienced noise problems early in the run period, but the difficulty was solved by increasing the discriminator thresholds on all the wire chamber outputs.

The wire chamber cuts provide information on the chamber efficiencies. The efficiency of a single chamber can be written as (using WC5 as an example),

$$\mathrm{Eff5} = \frac{\mathrm{WC1 \cdot WC3 \cdot WC4 \cdot WC5}}{\mathrm{WC1 \cdot WC3 \cdot WC4}}$$

where WCn indicates a valid firing in both the x and y coordinates of of the n^{th} chamber. The total wire chamber efficiencies are then the product of the individual efficiencies, and was typically ~ 90%. For the π^- data, MOLLI also removed those events for which F2X did not fire or for which multiple hits were registered.

The program MOLLI then transfers the data which has passed these

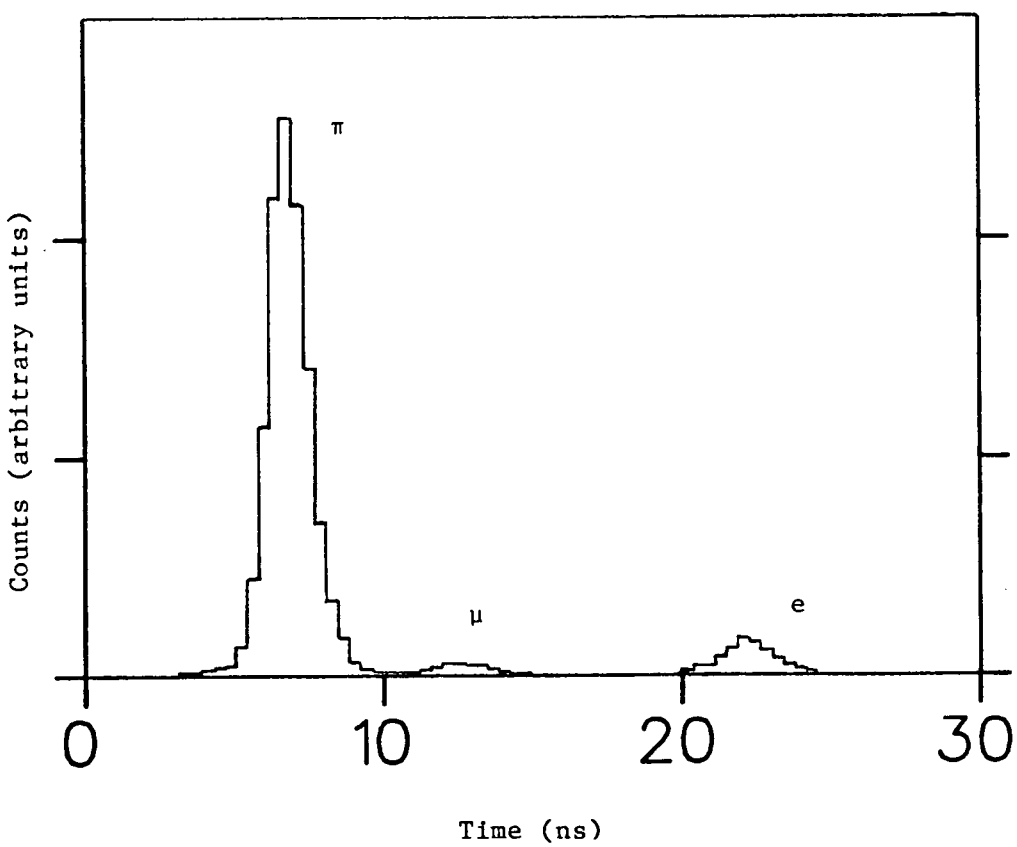

Fig. 3.1 Typical Time-of-Flight (TOF) histogram for π^- in the M13 channel

cuts to a file readable by the package QQDMP developed by B.M. Barnett (Bar 85). This package allows the determination of the magnetic transfer coefficients of the spectrometer for the quantity $\delta = (\Delta p/p)*100\%$ and for peak fitting of the resulting spectra

3.1.2 Coefficients

There are two different sets of tracing coefficients that are needed in the analysis. For producing pictures of the beam spot on the target, a set of coefficients for tracing the pion path back through the front two wire chambers to the scattering target is required. There is the QT2 magnet in between WC1 and WC3, so the trace back is not a simple linear trace back. However, since the magnetic element is not a dipole, it is assumed that there will not be a large δ dependence in the traceback. The other set is the spectrometer's magnetic transfer coefficients. These have very important δ dependencies as the system these coefficients describe contains the spectrometer dipole, BT.

3.1.2.1 Front End Coefficients

The target coordinates that are desired are the positions in x and y (X0 and Y0) and the angles to the spectrometer's central ray in the x- and y-planes (TH0 and PH0). The tracebacks have the form

$$(X0 \text{ or } TH0) = a_1 \cdot X1 + a_3 \cdot X3$$

and

$$(Y0 \text{ or } PH0) = b_1 \cdot Y1 + b_3 \cdot Y3 \ .$$

Two special targets constructed of nichrome slats 3 mm wide set about 10 mm apart, one target with horizontal slats, one with vertical, are placed at the scattering target and spectrometer data is taken. In analyzing

this data, one adjusts the coefficients for XO and YO to obtain the correct slat positions. The THO and PHO coefficients can be obtained by forcing the angular positions of the slats as viewed by WC1 to be consistent with the pion trajectory's physical positions at the target and WC1. These coefficients were not the result of a rigorous fitting procedure, but obtained by hand to the point where they are adequate for use. Substantial effort was not spent on finding the front traceback to a high precision as they are used for target cuts where some small inaccuracy is tolerable, but not for δ determination in which good precision is desired.

3.1.2.2 Spectrometer Coefficients

The focal plane of the spectrometer lies at an angle of 72 degrees to the central ray of the spectrometer and is beyond the two rear wire chambers. The positions in the back wire chambers by themselves will not give a good indication of the energy spectrum of the scattered pions. To produce a good spectrum, the information of the front two chambers must be used to, in effect, create a software spectrometer. For each back end chamber, the value of δ can be determined from the x coordinate in the back chamber and a set of front end coordinates. The front end coordinates can be the x and y positions in WC1 and WC3, or it can be the set of target coordinates described in 3.1.2.1.

Raytracing with the target coordinates was used by (Sob 84a). This method has the advantage that it usually requires a fairly small coefficient set and that a good starting point for the coefficients to first order in δ can be taken from the program TRANSPORT. However, higher order terms can be very important in obtaining a good final resolution.

Also, an accurate traceback to determine the target coordinates is very important, especially for the angular terms which are somewhat more difficult to obtain. During the summer of 1984, a drift chamber was tested at the WC1 location replacing the first two wire chambers. As the drift chamber is located before the first quadrupole, only a simple linear traceback to the target is needed and can provide target coordinates with a high degree of precision, removing some of the disadvantages of the target coordinate approach.

The front chamber information can be employed directly to obtain the transfer coefficients in the package QQDMP. The parameterization is of the form (using WC5X as an example),

$$WC5X = A + B*\delta_5 + C*\delta_5^2$$

with A, B, and C of the form

A = (polynomial of order m_0 in front-end coordinates)

B = (polynomial of order m_1 in front-end coordinates)

C = (polynomial of order m_2 in front-end coordinates) .

In practice, the expansion is taken at most to third order, that is m_0=3, m_1=2, and m_2=1. The parameterization can be meaningfully inverted to obtain δ_5. In a similar manner, δ_4 can be obtained. The parameterizations for WC4Y and WC5Y do not yield reliable δ information as there is little δ dependence in the y-direction.

Two types of data can be used to find the transfer coefficients. A CH_2 run at some spectrometer angle where the 2^+ (4.44 MeV) state in carbon can be expected to be sizable can be done with the spectrometer and channel settings set to experimental values. In QQDMP, one then defines the elastic and inelastic peak locations and attempts to minimize

the peak widths. The two peaks are weighted such that the peak heights are approximately equal so that one region of the energy spectrum is not favored more in the fitting than other regions. The elastic peak from the hydrogen can also be included in the fitting, but should be weighted less than the carbon peaks as one expects the hydrogen peak to be broader than the carbon peaks due to kinematics.

The method above was used to determine the transfer coefficients for this experiment. Perhaps a better approach is to take CH_2 spectra at some angle with the spectrometer at the experimental field settings, but then vary the channel settings in a systematic manner to maintain a good channel tune to shift the energy of the elastic carbon peak in the spectrometer. The elastic peaks from different known incident energies are then used in the minimization procedure. One can then be more confident about the constancy of the peak shape over the spectrometer acceptance. This method was employed in the double-charge-exchange (DCX) runs in December, 1984 (Hes 85).

To analyze the π^- data, the information from the F2 counter must be used to counteract the degrading of the resolution resulting from the wider F1 slit setting (25 mm versus 6 mm for the π^+ data). Using the same transfer coefficient set derived above for the π^+ data, one examines a scatter plot of F2 position against the calculated δ. A correction of 2% per wire is made to the calculated δ to remove the F2 dependence in the scatterplot, that is,

$$\delta_{corr} = \delta_i + (F2 - 8)*.2 \qquad i = 4 \text{ or } 5$$

such that for the center (wire 8) of the F2 counter no correction is made to the δ calulated. The same correction is made for δ_4 and δ_5. The F2

wire spacing is 1/10 inch, indicating that the channel dispersion at F2 is 2% per inch or 1.25 cm/% which is consistent with (Ora 81). This correction for the F2 position leads to a best resolution obtained of ~ 1.0 MeV for the π^- data as compared to ~ 1.1 MeV for the π^+.

3.1.3 Cuts in QQDANA

QQDANA is a version of QQDMP which is optimized for analyzing the data, but cannot be used for coefficient determination. Two values of δ are determined from the transfer coefficients, one value from each back end chamber. Ideally, $\delta_4=\delta_5$, but in practice this is not true. If a pion decays to a muon in the spectrometer, the muons path will depart from the pion's trajectory at some angle which is limited by kinematics to <18 degrees in the lab frame (see for example Appendix D in (Tac 84)). If the muon remains in the spectrometer so that δ's are calculated for its path, the resulting values of δ found may be substantially different. If the calculated difference in the δ's was more than 1%, the event was cut (the DDIF cut). Using the value of δ_4, the trajectory to WC5 can be predicted, and a polar angle between the actual trajectory and that predicted can be calculated. If this angle is too large, the event is cut (the ANGL cut). The DDIF and ANGL cuts are overlapping to a large extent, but it is useful to employ them both. Typical cuts are shown in Fig. 3.2a) and Fig. 3.2b). The cuts efficiencies are calculated from data in the region of the elastic peak.

The calcium targets available for this experiment were not large enough to intercept the entire beam. To determine the beam fraction passing through the target, a traceback to the target was necessary. The CH_2 target used for reference measurements was large enough to intercept

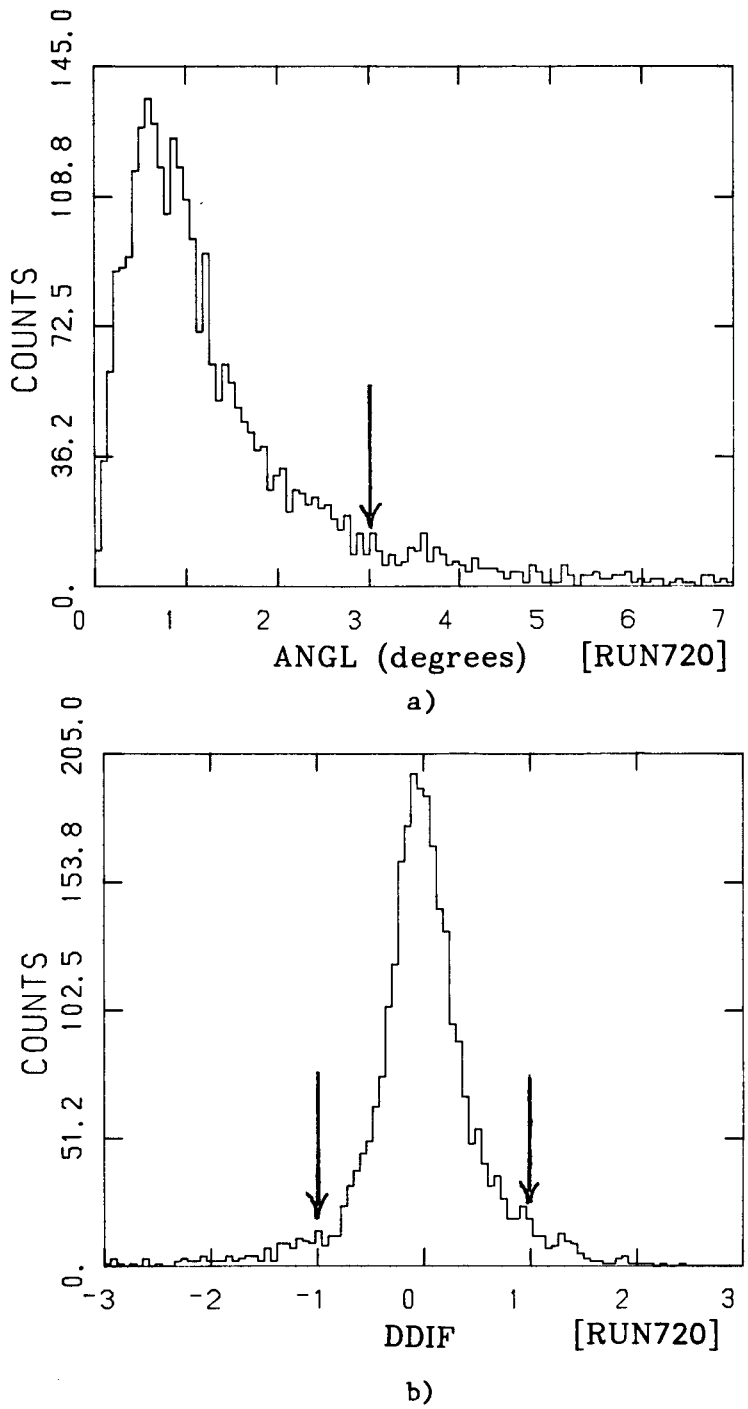

Fig. 3.2 Showing a) the position of the ANGL cut, and b) the positions of the DDIF cuts.

the entire beam. Analyzing the CH_2 data with the relevant calcium target cuts at each angle, in comparison to a CH_2 analysis with no target cuts, established for each angle the beam fraction passing through the target. The assumption is made that the beam spot does not change substantially between runs at the same angle.

3.1.4 The Spectrometer and Target Angles

The spectrometer angle for each measurement is read from an angle indicator on the supporting track of the spectrometer. The accuracy of this angle depends upon the accuracy with which the track is laid down before each experimental period, the accuracy to which the pion beam follows the assumed path, and the accuracy to which the original angle markings were established. A method of calibrating any possible angle offset in the reading is available in the CH_2 target data. Due to the small proton mass (relative to the ^{12}C nucleus), the energy of the scattered pion will vary greatly; from 50 MeV at 0° to 25.4 MeV at 180°. Spectrometer data was taken at nominal angles of 80° and 90° on the left and right side of the beam. From these spectra, the peak energies of pions elastically scattering off protons are obtained. By adjusting the scattering angle, these peak energies are aligned with the smoothly varying curve of energy versus angle expected from kinematics. By this procedure, it is found that there is an angle offset of 2° right necessary to smooth the peak location data. That is to say, an 80° (left) data point is actually at 78° (left) and an 80° (right) at 82° (right).

This offset has some effect on the target angle as well. The target is positioned in the transmission mode so that all the pions traverse the full target. The nominal target angle is then given by

$$\theta_{tgt} = \frac{\theta_{track}}{2}$$

but is modified by the offset to become

$$\theta_{tgt} = \frac{\theta_{track}}{2} + (-)\ 2°$$

for right (left) settings.

3.2 Peak Fitting

As mentioned above, QQDANA provides a means of fitting spectra. These spectra can contain one or more peaks of gaussian or sum-of-gaussian shape (that is, two gaussians summed to fit a single peak, one gaussian of large width, one narrow). Parameters describing the peak seperation, width, and position can be fixed or allowed to vary within optional limits. The peak fitting is crucial for the ^{48}Ca data, where the contribution of the ^{16}O contaminant must be estimated.

The ^{40}Ca and ^{12}C were straightforward to fit. There was negligible contamination in the ^{40}Ca target and the nearest inelastic states are 3.8 MeV away. The ^{12}C data is from the CH_2 target. The proton peak is well separated from the ^{12}C ground state at all angles measured and the first excited state in ^{12}C is at 4.44 MeV. The resulting ^{12}C and ^{40}Ca spectra are very clean (see Fig. 3.3a) and 3.3b)), and the peak areas and locations could be reliably fitted.

The ^{40}Ca fitted mean and width can be used to estimate the ^{48}Ca mean and width. This can be done by correcting for the different ionization losses in the two targets for the mean, and by unfolding the estimated difference in target multiple scattering for the width (multiple scattering contribution to the width is ~ 25% of the ionization losses). The ^{16}O contamination peak is taken to have the same width as

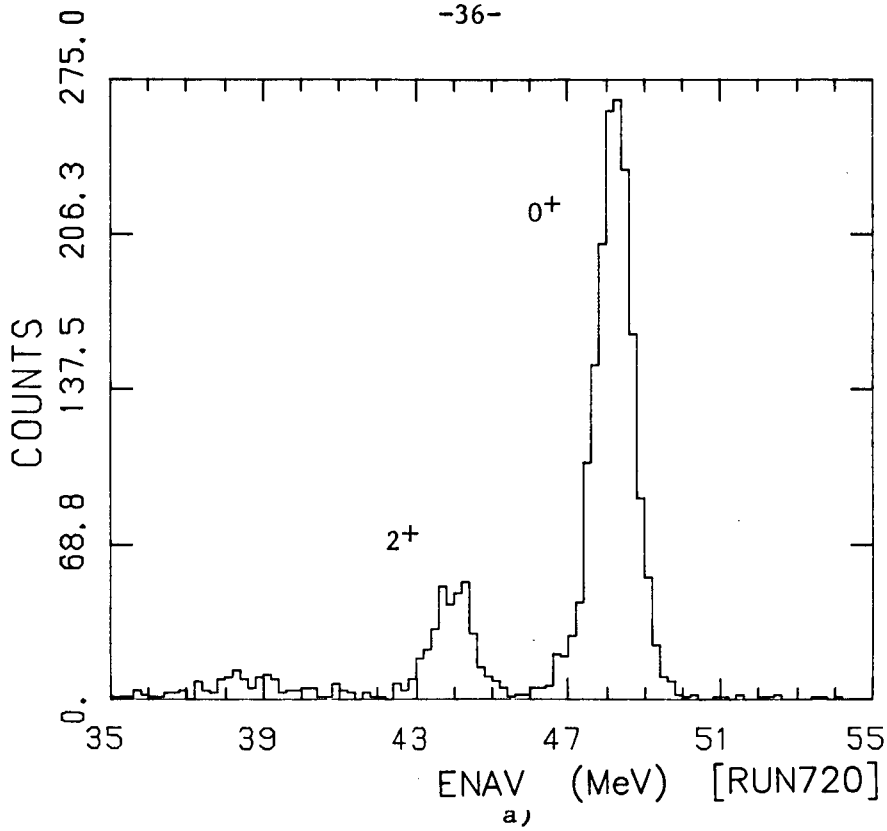

a)

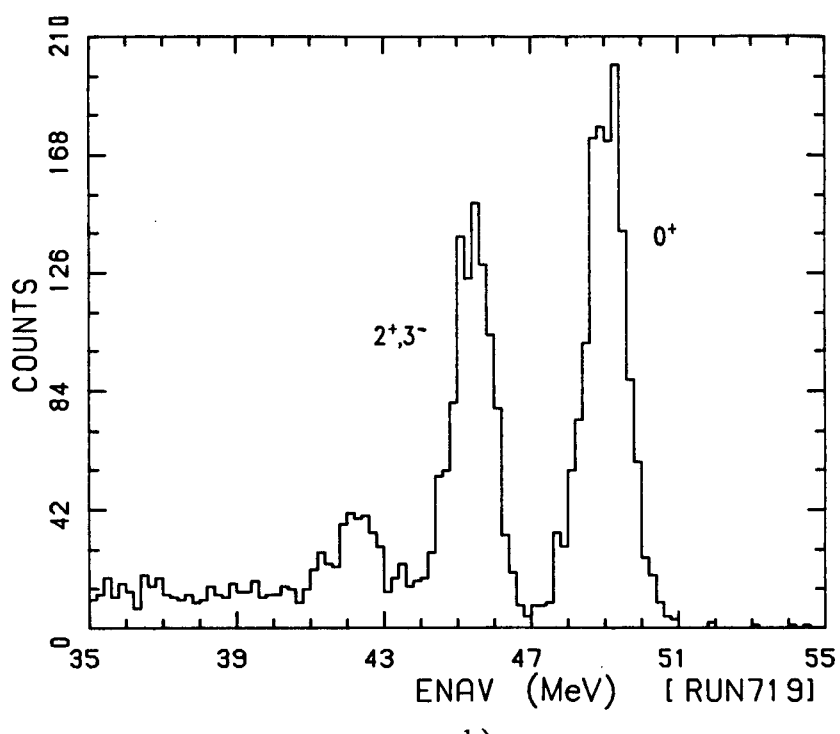

b)

Fig. 3.3 Typical spectra for π^+ at 122 degrees for a) CH_2, and b) ^{40}Ca. ENAV is the average energy calculated from wire chambers 4 and 5.

the ^{48}Ca peak and its location is estimated from the kinematic energy differences between ^{16}O and ^{48}Ca. These estimates provide a good starting point for the fit. It has been assumed that the primary contaminant is ^{16}O. ^{12}C and ^{14}N are other possibilities, however at the most backward angles these contaminants would have been better resolved (1.8 and 1.5 MeV separation with ^{48}Ca as compared to 1.2 MeV for ^{16}O at 130°) than the data and the resulting fits indicated. For a sample ^{48}Ca spectrum see Fig. 3.4.

Separate fitting of the ^{16}O and ^{48}Ca peaks is only possible at $\theta_{spec} > 90°$ where the peak separation and relative peak heights are adequate for reliable fits. From the peak areas found for the ^{16}O, the target density of ^{16}O is found to be $4.55 \pm .32$ (10^{20}) nuclei/cm^2. To calculate this density, reference $\pi^{\pm}$ - ^{16}O cross-sections are required. The π^+ reference is taken from (Bar 85) and the π^- from (Daw 81)

There is sufficient inelastic data in the Ca data that one might expect to be able to extract inelastic cross-sections, however several problems with the inelastic data were encountered. In ^{40}Ca, the 2^+ state of interest is only 170 keV from a possibly strong 3^- state and is thus unresolvable. Some preliminary analysis indicated that the cross-sections obtained are more consistent with the 3^- state than the 2^+ state. In ^{48}Ca, there is a strong 3^- state only 700 keV above the 2^+ (3.83 MeV) state and is again not easily resolvable. The presence of the oxygen contamination makes the fitting complicated and no consistent cross-sections could be extracted for the inelastic states. Due to these problems, the inelastic data is not presented here.

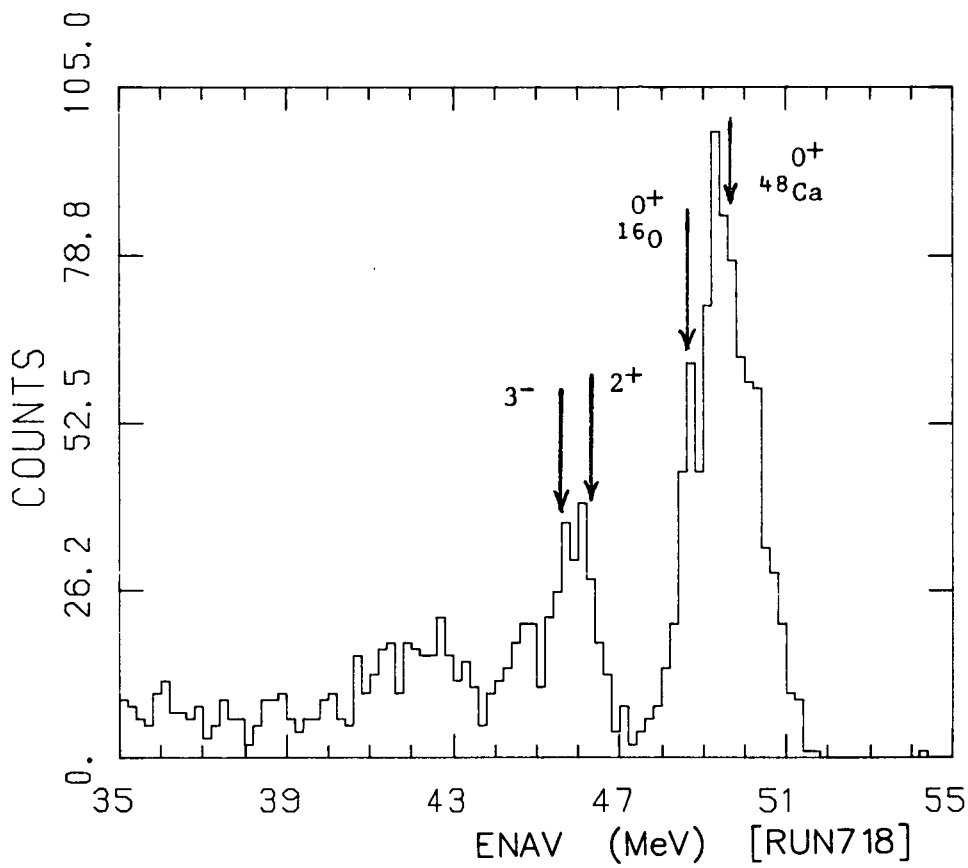

Fig. 3.4 Typical spectra for π^+ at 122 degrees for ^{48}Ca

3.3 Absolute Cross-Sections

The absolute differential cross-section may be calculated from

$$\left(\frac{d\sigma}{d\Omega} \right)_{c.m.} = \frac{N_{peak} \cdot 10^{27}}{\phi \cdot N_{tgt}} \cdot g(\theta) \cdot J(\theta) \qquad \left(\frac{mb}{sr}\right)$$

where

N_{peak} is the fitted peak area

ϕ is the total beam flux BM1•BM2

N_{tgt} is the number of scattering centers in the target per cm^2

$J(\theta)$ is the Jacobian converting from the lab to c.m. frame

and $g(\theta)$ contains all the normalization factors. It can be expressed as

$$g(\theta) = \frac{\cos(\theta_{tgt})}{\Delta\Omega} \cdot \frac{1}{WC} \cdot \frac{1}{\pi\mu e} \cdot \frac{1}{\pi\text{-dec}} \cdot \frac{1}{Tgt} \cdot MHC \cdot PS$$

where

θ_{tgt} is the target angle corrected for offsets

$\Delta\Omega$ = 16 msr is the estimated spectrometer solid angle

WC is the total wire chamber efficiency

$\pi\mu e$ is the pion beam fraction

π-dec = .717 is the fraction of pions traversing the 2.38 m path through the spectrometer without decaying

Tgt is the target cut efficiency

MHC is the multiple hits correction

and

PS is the phase-shift normalization.

The value taken for the solid angle is an estimate based on previous group work. The pion decay factor takes as the flight path the nominal central path through the spectrometer to the last wire chamber. The exact central ray is not known well. However, any uncertainties in

the decay factor as well as the solid angle are taken to be absorbed into the overall normalization error of the data (taken as 10%). Differences in these factors between π^+ and π^- can be treated in the phase shift normalization factor.

The hydrogen cross-sections extracted from the CH_2 data can be compared to the output of the dial-in program SAID (Arn 82). SAID calculates cross-sections from phase shift obtained from $\pi^{\pm}p$ experiments. The various experiments are not in excellent agreement, so that the calculated cross-sections cannot be taken as perfect. They are, however, the best available at this time. Results from SAID are shown in Fig. 1.1b). The forward angle hydrogen data were compared to SAID outputs as they are close enough to the carbon peak such that the cuts on the carbon should have the same effect on the hydrogen peak. Care is taken to ensure that there is no significant carbon inelastic background under the hydrogen peak. The statistical errors are at the 5% level for the π^+ and about 7% for the π^- data. It is found that a 15% downward normalization is required for the π^+ results to agree with SAID, but that no normalization is required for the π^-.

The MHC factor is needed to correct for the occurence of multiple pions per primary beam burst, which becomes more common as the pion beam flux rises. To correct for this, consider a beam burst in which two pions arrive at the target. For the π^+ data, the beam monitor BM1•BM2 will register only one pulse. However, as there are two pions, the probability that one will be scattered into the spectrometer is doubled, and hence the effective flux is increased, reducing the cross-section. For π^-, the F2 counter is likely to register two hits and thus reject the data completely. The effective flux is thus lowered, raising the resulting

cross-sections. These effects are still rather small at the pion rates used in the experiment. Average MHC correction factors are .97 for π^+ and 1.02 for π^-.

The cross-section errors may then be calculated by adding in quadrature all terms contributing uncertainty to the cross-section except for those errors which are absorbed into the normalization error. The error can then be written as

$$\frac{\Delta\left(\frac{d\sigma}{d\Omega}\right)_{c.m.}}{\left(\frac{d\sigma}{d\Omega}\right)_{c.m.}} = \left[\frac{1}{N_{peak}} + (\tan\theta_{tgt}\cdot\Delta\theta)^2 + \left(\frac{\Delta WC}{WC}\right)^2 + \left(\frac{\Delta\pi\mu e}{\pi\mu e}\right)^2 + \left(\frac{\Delta cuts}{cuts}\right)^2 + \left(\frac{\Delta N_{tgt}}{N_{tgt}}\right)^2 + \left(\frac{\Delta flux}{flux}\right)^2 \right]^{1/2}$$

with

$$\Delta\theta = 1^\circ \ (\ \pi/180 \ \text{radians})$$

$$\frac{\Delta\pi\mu e}{\pi\mu e} = 1\% \quad \text{from estimating the beam fraction}$$

and

$$\frac{\Delta flux}{flux} \sim 2\% \quad \text{at the forward angles.}$$

The angular error is estimated from the uncertainty in the angle offset and uncertainty in the positioning of the target. The cuts errors are supplied by outputs from fitting with QQDANA and can be estimated, as can the wire chamber error by

$$\frac{\Delta Eff}{Eff} = \left[\frac{1-Eff}{N} \right]^{1/2} \sim 1\% \text{ or less typically}$$

with N being the number of data points in the cut region and Eff the cut efficiency.

At forward angles (<60°) the housing of the WC1 starts to intercept the beam before it can reach BM2, thus BM1•BM2 is no longer reliable as a

measure of the flux. The flux error indicated is an estimate of the uncertainties of the beam fluxes scaled from the muon counters, and is taken to be 2%, the approximate stability limit of the muon counters.

The density of scattering centers, N_{tgt}, has negligible error for the CH_2 and ^{40}Ca targets as the areas and masses are well known. This is not the case for the ^{48}Ca target where the ^{16}O content is important. However, even for ^{48}Ca this error is less than 1%.

A major contribution to the ^{48}Ca errors comes from the uncertainty of the ^{16}O contribution to the elastic peak area. For the ^{48}Ca errors, the fractional error in the peak area is not

$$\left(\frac{1}{N_{peak}} \right)^{1/2}$$

but becomes

$$\left(\frac{\Delta N_{peak}}{N_{peak}} \right) = \left[A_{sum} + \left(\Delta A_{16} \right)^2 \right]^{1/2}$$

where A_{sum} is the total peak area including the contamination, and ΔA_{16} is the error in the estimated ^{16}O area.

The resulting differential cross-sections and their errors are shown in Tables 3.1 to 3.3. The ^{12}C results compare very well with the data of (Sob 84a), agreeing to better than 5% for the most part. The $\pi^{+-}{}^{40}Ca$ data do not agree well with the only previous published cross-sections of (Pre 81). Agreement with the unpublished data of (Daw 81) is reasonable, being the best at angles less than 100°.

It should be noted that effects due to the finite spectrometer acceptance and angular width of the pion beam have not been accounted for in finding the differential cross-sections. These effects will be most prominent where the cross-section changes rapidly with angle, that is, at

	θ_{cm} (deg)	$d\sigma/d\Omega$ (mb/sr)
π^+	38.6	7.01 ± 0.27
	48.7	4.20 ± 0.15
	58.8	2.56 ± 0.10
	68.9	2.52 ± 0.10
	78.9	3.64 ± 0.14
	83.0	3.90 ± 0.14
	89.0	4.77 ± 0.20
	93.0	5.01 ± 0.14
	102.9	5.47 ± 0.24
	112.9	6.38 ± 0.26
	122.8	6.18 ± 0.29
	130.7	5.75 ± 0.30
π^-	38.6	20.44 ± 0.76
	48.7	8.63 ± 0.36
	58.8	3.15 ± 0.13
	68.9	2.26 ± 0.11
	78.9	3.27 ± 0.15
	83.0	3.90 ± 0.17
	89.0	5.38 ± 0.27
	93.0	5.63 ± 0.27
	102.9	6.56 ± 0.28
	112.9	6.90 ± 0.35
	122.8	6.59 ± 0.38
	130.7	6.13 ± 0.38

Table 3.1 Measured $\pi^{\pm}$ differential cross-sections for ^{12}C at 49.5 MeV.

	θ_{cm} (deg)	$d\sigma/d\Omega$ (mb/sr)
π^+	38.2	37.40 ± 1.84
	48.2	20.72 ± 0.78
	58.2	14.99 ± 0.45
	68.3	14.60 ± 0.50
	78.3	12.84 ± 0.54
	82.3	13.59 ± 0.38
	88.3	11.82 ± 0.51
	92.3	10.63 ± 0.27
	102.3	7.24 ± 0.32
	112.3	5.04 ± 0.23
	122.2	3.84 ± 0.20
	130.2	4.27 ± 0.25
π^-	38.2	109.5 ± 5.4
	48.2	38.24 ± 1.38
	58.2	20.63 ± 0.56
	68.3	20.68 ± 0.83
	78.3	16.62 ± 0.93
	82.3	16.20 ± 0.60
	88.3	9.98 ± 0.57
	92.3	8.29 ± 0.35
	102.3	2.61 ± 0.17
	112.3	0.51 ± 0.06
	122.2	1.49 ± 0.13
	130.2	2.81 ± 0.19

Table 3.2 Measured $\pi^{\pm}$ differential cross-sections for ^{40}Ca at 49.5 MeV

	θ_{cm} (deg)	$d\sigma/d\Omega$ (mb/sr)
π^+	38.1	44.63 ± 2.78
	48.2	20.97 ± 1.37
	58.2	10.90 ± 0.47
	68.2	9.66 ± 0.64
	82.2	11.44 ± 0.47
	92.2	8.78 ± 0.34
	102.2	4.74 ± 0.51
	112.2	3.15 ± 0.35
	122.2	2.69 ± 0.33
	130.2	2.92 ± 0.33
π^-	38.1	111.7 ± 6.7
	48.2	45.88 ± 2.67
	58.2	34.28 ± 1.13
	68.2	30.03 ± 1.71
	82.2	15.92 ± 0.70
	92.2	5.38 ± 0.42
	102.2	0.67 ± 0.35
	112.2	2.48 ± 0.37
	122.2	7.58 ± 0.56
	130.2	9.09 ± 0.67

Table 3.3 Measured $\pi^{\pm}$ differential cross-sections for ^{48}Ca at 49.7 MeV

very forward angles and in the diffractive region.

3.4 Cross-Section Ratios.

For obtaining information on the neutron density differences between ^{48}Ca and ^{40}Ca through the use of fourier-bessel terms in the neutron density, it is desirable to fit ratio data. The ratio data will be free of normalization errors and effects due to common errors such as target angle errors and beam flux errors.

The absolute ^{48}Ca cross-sections have been given above, so that the ratio information is in a sense a restatement of results. However, the data is presented in this manner as the analyses for ^{40}Ca and ^{48}Ca are similar, but not identical, the differences being mainly in the effects of different target sizes.

The cross-section ratio, R, is then

$$R = \frac{48_\sigma}{40_\sigma}$$

with σ denoting the differential cross-section. The error in R is given by

$$\frac{\Delta R}{R} = \left[\left(\frac{\Delta^{48}\sigma}{48_\sigma} \right)^2 + \left(\frac{\Delta^{40}\sigma}{40_\sigma} \right)^2 - 2 \cdot \left(\text{C.E.} \right)^2 \right]^{1/2}$$

where C.E. is the sum in quadruture of common errors; target angle errors, pion beam fraction error, and the flux error. The factor of 2 compensates for these errors appearing once each in the ^{40}Ca and ^{48}Ca calculations. Wire chamber errors are not subtracted as WC1 and WC3 encountered efficiency problems during running and were not always stable (their error contribution is small anyway). The calculated ratios and their errors are given in Table 3.4.

	θ_{cm} (deg)	$^{48}\sigma/^{40}\sigma$
π^+	38.2	1.193 ± 0.060
	48.2	1.012 ± 0.066
	58.2	0.727 ± 0.033
	68.3	0.662 ± 0.046
	82.3	0.842 ± 0.034
	92.3	0.826 ± 0.029
	102.3	0.655 ± 0.072
	112.3	0.625 ± 0.071
	122.2	0.701 ± 0.085
	130.2	0.684 ± 0.077
π^-	38.2	1.020 ± 0.048
	48.2	1.120 ± 0.067
	58.2	1.662 ± 0.054
	68.3	1.452 ± 0.090
	82.3	0.983 ± 0.049
	92.3	0.649 ± 0.053
	102.3	0.257 ± 0.133
	112.3	4.863 ± 0.915
	122.2	5.087 ± 0.518
	130.2	3.235 ± 0.269

Table 3.4 $\pi^{\pm}$ differential cross-section ratios for Calcium

Chapter IV

THE THEORY

In this chapter, some of the details of the theory used in the description of pion-nucleus scattering will be given. The optical potential and the point in the Klein-Gordon equation at which the potential is inserted to describe the scattering of the pions will be discussed. Application of the theory to the actual data is left to Chapter 5.

4.1 Scattering Theory

The scattering of a particle by a potential V(r) can be described in the Born approximation which gives the differential cross-section of scattering as

$$\frac{d\sigma}{d\Omega} \sim | V(q) |^2$$

where

$$V(q) = \langle \psi_f | V(r) | \psi_i \rangle$$

$$V(q) = \int e^{i\vec{q}\cdot\vec{r}} V(r) \, d^3r \, .$$

ψ_f and ψ_i are the final and incident particle wavefunctions which are taken to be plane waves of momenta k_f and k_i and

$$\vec{q} = \vec{k}_i - \vec{k}_f$$

is the momentum transfer.

For the case of a nucleus, V(r) is the convolution of the interaction of the particle with a point nucleon and the nucleon distribution

$$V(r) = \int U(r-r')\ \rho(r')\ d^3r' \quad .$$

From the properties of a Fourier transform of a convolution

$$\tilde{F}\ \{\ a(r-r')\ b(r)\ \} = a(q)\ b(q)$$

the result

$$\frac{d\sigma}{d\Omega} \sim |\ U(q)\ \rho(q)\ |^2$$

is obtained. Thus, both the particle-nucleon interaction and the nucleon distribution are, in general, needed to describe the reaction.

4.2 The Klein-Gordon Equation

The equation used to describe the potential scattering of a relativistic spin zero particle upon a nucleus is the Klein-Gordon equation. The free particle Klein-Gordon equation is given by

$$(\ E^2 - p^2\ )\ \psi = m^2\ \psi$$

where E is the total particle energy, m its mass and p its 3-momentum. If one assumes that the nuclear potential V_n can be included along with the static Coulomb potential V_c with the energy E, the equation can then be expressed as

$$((\ E - V_c - V_n)^2 - p^2\ )\psi = m^2\ \psi$$

or

$$(\ E^2 + V_c^2 + V_n^2 - 2EV_c - 2EV_n - V_cV_n - V_nV_c - p^2\ )\ \psi = m^2\ \psi\ .$$

The V_n^2 term and the Coulomb-nuclear cross terms are usually neglected.

The final form of the equation is then

$$(\ E^2 + V_c^2 - 2EV_c - 2EV_n - p^2\ )\ \psi = m^2\ \psi \quad .$$

The term $2EV_n$ is the optical potential to be discussed below.

4.3 The Optical Potential

A description of the pion-nucleus interaction may be developed in a manner analogous to the interaction of photons with matter. For the photon interaction, the matter through which the photon propagates is modified with respect to the vacuum by its refractive index. In a like manner, the nuclear matter through which the pion propagates is given a complex index of refraction so that it can both scatter and absorb the incident pions.

One purpose of developing a pion-nucleus optical potential is to obtain a semi-phenomenological model, based on theoretical considerations, which can successfully describe data. Ideally, it should be able to describe a wide range of $\pi^{\pm}$ data with parameters which vary slowly and smoothly with energy with no A dependence over an energy range from negative energies (pionic atoms) to low energies of the order 50 MeV where the Δ_{33} is not yet overwhelmingly dominant. To this extent, the SMC potential (Str 79, Str 80, Car 82) discussed below is fairly successful, at least for π^{+} data. It is not the only possible potential form but incorporates many features which have been demonstrated to be useful in obtaining good data fits.

For the low energy region, the pion-nucleus scattering amplitude can be written in the form

$$f = b_0 + b_1 \vec{t}\cdot\vec{\tau} + (c_0 + c_1 \vec{t}\cdot\vec{\tau})\vec{k}\cdot\vec{k}' - i(d_0 + d_1 \vec{t}\cdot\vec{\tau})\vec{\sigma}\cdot(\vec{k}\times\vec{k}')$$

where $\vec{k}$, $\vec{k}'$ are the momenta of the incident and scattered pion, b_0, b_1, c_0, c_1, d_0, and d_1 are constants which are related to the s-wave pion-nucleon scattering length and p-wave scattering volume. The constants b_0, c_0, and d_0 are referred to as isoscaler while b_1, c_1, and

d_1 are isovector. The operators $\vec{t}$, $\vec{\tau}$, and $\vec{\sigma}$ are respectively the pion isospin, the nucleon isospin, and the nucleon spin. In most studied nuclei, the nucleus tends to be spin saturated (Eis 80) so that the spin term can be ignored.

The finite widths of pionic atom levels imply that absorption of the pion must be included in the potential. The absorption is assumed to predominantly occur on nucleon pairs (absorption on a single nucleon being strongly suppressed by energy conservation). The parameterization of the absorption in the optical potential is then in terms of the square of the nucleon density.

It has been noted that to better explain pion data, the potential must be expanded to second order in the multiple scattering series (Eri 66). In second order, the nuclear pair correlations produce two effects. First, the s-wave parameter b_0 is replaced by an effective s-wave scattering length in the nucleus, $\overline{b}_0$, given by

$$\overline{b}_0 \simeq b_0 - \frac{3}{2\pi}\left(b_0^2 + 2b_1^2 \right)k_F$$

where k_F is the Fermi momentum, here taken to be 1.4 fm^{-1}. Second, the nuclear pair correlations produce an effect analogous to the so-called Lorentz-Lorenz effect which is caused by the scattering of electromagnetic waves in a dense, polarizable medium. This effect introduces a term in the potential referred to as the Lorentz-Lorenz-Ericson-Ericson (LLEE) term and its strength in the optical potential is determined by the parameter λ.

The resulting optical potential including second order effects is then of the form

$$2\,\omega\,U_{opt} = -4\pi\,\Big[\,p_1\,b(r) + p_2\,B(r) + \nabla^2\Big(\frac{(p_1-1)c(r)}{2p_1} + \frac{(p_2-1)C(r)}{2p_2}\Big) - \vec{\nabla}\cdot\Big(\frac{L(r)}{1+\frac{4\pi\lambda}{3}L(r)}\Big)\vec{\nabla}\,\Big]$$

with

$$b(r) = b_0\,\rho(r) - \varepsilon_\pi\,b_1\,\delta\rho(r)$$

$$c(r) = c_0\,\rho(r) - \varepsilon_\pi\,c_1\,\delta\rho(r)$$

$$B(r) = B_0\,\rho^2(r) - \varepsilon_\pi\,B_1\,\rho(r)\,\delta\rho(r)$$

$$C(r) = C_0\,\rho^2(r) - \varepsilon_\pi\,C_1\,\rho(r)\,\delta\rho(r)$$

$$L(r) = p_1^{-1}\,c(r) + p_2^{-1}\,C(r)$$

where

$\varepsilon_\pi = \pm 1$ is the pion charge ,

and

$$p_1 = \frac{1+\frac{\omega}{m}}{1+\frac{\omega}{mA}}$$

and

$$p_2 = \frac{1+\frac{\omega}{2m}}{1+\frac{\omega}{2mA}}$$

are kinematic factors resulting from the transformation from the pion-nucleon to the pion-nucleus center-of-mass frame. The density terms are

$$\rho(r) = \rho_n(r) + \rho_p(r)$$

and

$$\delta\rho(r) = \rho_n(r) - \rho_p(r)$$

with ρ_n, ρ_p, and ρ normalized to N, Z, and A respectively. The nucleon mass is m (~ 931 MeV) and ω is the total center-of-mass energy.

The terms in $\nabla^2\rho^2$ and $\nabla^2\rho$ are a consequence (Thi 76) of the transformation of the $\vec{k}\cdot\vec{k}'$ factor in the p-wave term of the scattering amplitude from the pion-nucleon to the pion-nucleus center-of-mass system. It is referred to as the angle transformation. B_0 and C_0 are the isoscaler absorption parameters. The isovector absorption factors, B_1 and C_1, are usually taken to be zero due to insufficient data to establish a reliable value.

The parameter set that is used as a starting point in the fitting of the calcium data (described in Chapter 5) is the parameter "SET E" of (Car 82). This parameter set was obtained as follows; Re B and Re C were taken from theoretical values, Im b and Im c from pion-nucleon phase-shift values modified by the effect of the Pauli principle, Im B and Im C from fits to absortion cross-sections, and Re b and Re c were adjusted to fit existing π^+ elastic scattering data. No π^- elastic scattering data was used in the fitting procedure for SET E as there were only limited data published at energies $\leq$ 50 MeV at the time. It is therefore reasonable to expect then that SET E may not adequately describe π^- scattering data. This has been shown to be true, at least for nuclei larger than carbon, in recent work (Tac 84, Sob 84, Gyl 84). The poor π^- description is also plainly evident in the data set of this experiment. The π^+ ^{40}Ca data of (Pre 81) was part of the data set used to obtain SET E. There is a discrepancy between the SET E fit and that data set as can be noted from (Car 82). The SET E parameters are shown in Table 4.1

SMC Optical Potential parameters	coefficients (Re + i Im)	
b_0 (fm)	-.061	.006
b_1 (fm)	-.13	-.002
c_0 (fm^3)	.70	.028
c_1 (fm^3)	.46	.013
B_0 (fm^4)	-.02	.11
C_0 (fm^6)	.36	.54
λ	1.4	

Table 4.1: The SET E optical potential parameters (Car 82)

Chapter V

RESULTS

The optical potential used to describe pion scattering in this thesis was discussed in Chapter IV. In addition to the optical potential, the nucleon and charge densities are required for the cross-section calculation to proceed. The form of density taken is the three parameter Fermi (3PF) form given by

$$\rho(r) = \rho_0 \frac{1 + w(r/c)^2}{1 + \exp((r-c)/t)}$$

where c is the half density radius , $4 \cdot \ln(3) \cdot t$ is the skin thickness, and w is the "wine-bottle" parameter. For ^{40}Ca and ^{48}Ca, the charge distribution parameters are taken from (Sin 73) and (Fro 68). The ^{48}Ca charge parameters have been adjusted slightly to reproduce the rms radius given in (Woh 81). By adjusting the c parameter of the distribution, the expected proton radii are reproduced. The neutron distribution of ^{40}Ca is taken equal to the proton distribution, which is consistent with α and proton experimental data. The 3PF parameters used in the analysis are shown in Table 5.1.

The computer code BRENDA was used to determine the optical potential through fitting the absolute ^{40}Ca data. BRENDA is a modified form of DWPI (Eis 76) that contains the SMC potential, and can handle a variety of density forms. The ratio fitting was done using the code of Krell and Thomas (Kre 68, Tho 81) in the form used in (Bar 85, Gyl 84) (referred to as the Krell code). The absolute cross-sections produced by these two codes agree to better than 2% over most of the angular range of

Nucleus	Parameter	Distribution				
		Charge	Proton	Neutron		
^{40}Ca	c (fm)	3.768	3.629	3.629		
	t (fm)	.5865	.5865	.5865		
	w	-.161	-.161	-.161		
				FIT B	FIT C	MIA
^{48}Ca	c (fm)	3.754	3.642	3.867	4.018	3.642
	t (fm)	.526	.526	.552	.529	.526
	w	-.03	-.03	-.03	-.03	-.03

Table 5.1 The Fermi distribution parameters used in this analysis. Note that for Krell code fitting, the charge distribution is set equal to the proton distribution. MIA refers to the Fermi parameter values used in the Fourier-Laguerre fits of section 5.2.2, while FIT B and FIT C refer to the best fit parameters from ratio fitting with those potentials to the whole angular range of the data set.

concern in this experiment. One of the main differences between the codes is the form taken for the charge density. In BRENDA, the charge parameters are separate from the proton parameters. In the Krell code, the charge distribution is set equal to the proton distribution for a Fermi density form. Differences between the codes should cancel to first order in the ratio calculation.

The method of solution employed by the optical codes is to numerically integrate the radial Klein-Gordon equation incorporating the nuclear and Coulomb potentials for each potential wave out to some predetermined radius. The resulting wavefunctions are then matched to the asymptotic Coulomb wavefunctions at that radius. In this manner, the phase shifts for each partial wave are determined, and thus the differential cross-sections.

In the thesis of (Gyl 84), some detail was given to considering the sensitivity of the ratios to the optical potential. Ratios in the diffractive region were shown to be very sensitive to the potential, and for that reason, data was taken only to ~ 105° for the sulpher and magnesium experiments. For the calcium isotopes, the diffractive minima occur at even smaller angles than the sulpher isotopes, so the angular range of the data would have to be greatly limited (maximum angle <95°) to reproduce the sulpher analysis methods. However, data points were taken to 130° as the inelastic data was originally also of interest. Thus, there may not be sufficient points at <95° for an extensive and reliable model independent analysis. One should note that the errors in the back angle ratio data tend to be large due to the contribution of the ^{16}O contamination. The optical potential sensitivity in the diffractive region should be somewhat reduced by these large errors so that it may be

possible to obtain consistency with the inclusion of the back angle data in the analysis.

5.1 Absolute Cross-Section Fits

As discussed in section 4.3, the SET E optical parameters are not expected to fit the π^- data very well. Also, the π^+-^{40}Ca data set of (Pre 81) is not fit well by the SET E calculation. The SET E calcution is shown in Fig. 5.1 and agrees well with the present π^+ data except at backward angles. There appears to be a normalization difference between this data set and the results of (Pre 81). As the author believes his data to be normalized correctly, then it must be concluded that the data of (Pre 81) is in error.

The energies used in these calculations are 49.5 MeV for ^{40}Ca and 49.7 MeV for ^{48}Ca. These energies correspond to the energy at the center of the targets assuming a 50 MeV incident beam energy. If the incident energy is not exactly 50 MeV, then the fit to the optical potential should compensate by adjusting the potential appropriately to mimic the energy effects.

From Fig. 5.1, it is seen that SET E does not describe the π^- data. This disagreement is consistent with trends observed in (Gyl 84,Sob 84a, Tac 84). To better reproduce the data, the parameters of the optical potential are adjusted through the minimization of the χ^2/ν defined by

$$\frac{\chi^2}{\nu} = \sum_n \left(\frac{\sigma_{calc} - \sigma_{exp}}{\Delta\sigma_{exp}} \right)^2$$

where the sum is over n data points and ν is the degree of freedom. The χ^2/ν of the SET E fit to the π^- and π^+ combined is 61. In order to constrain the potential better, the fitting is done to π^- and π^+

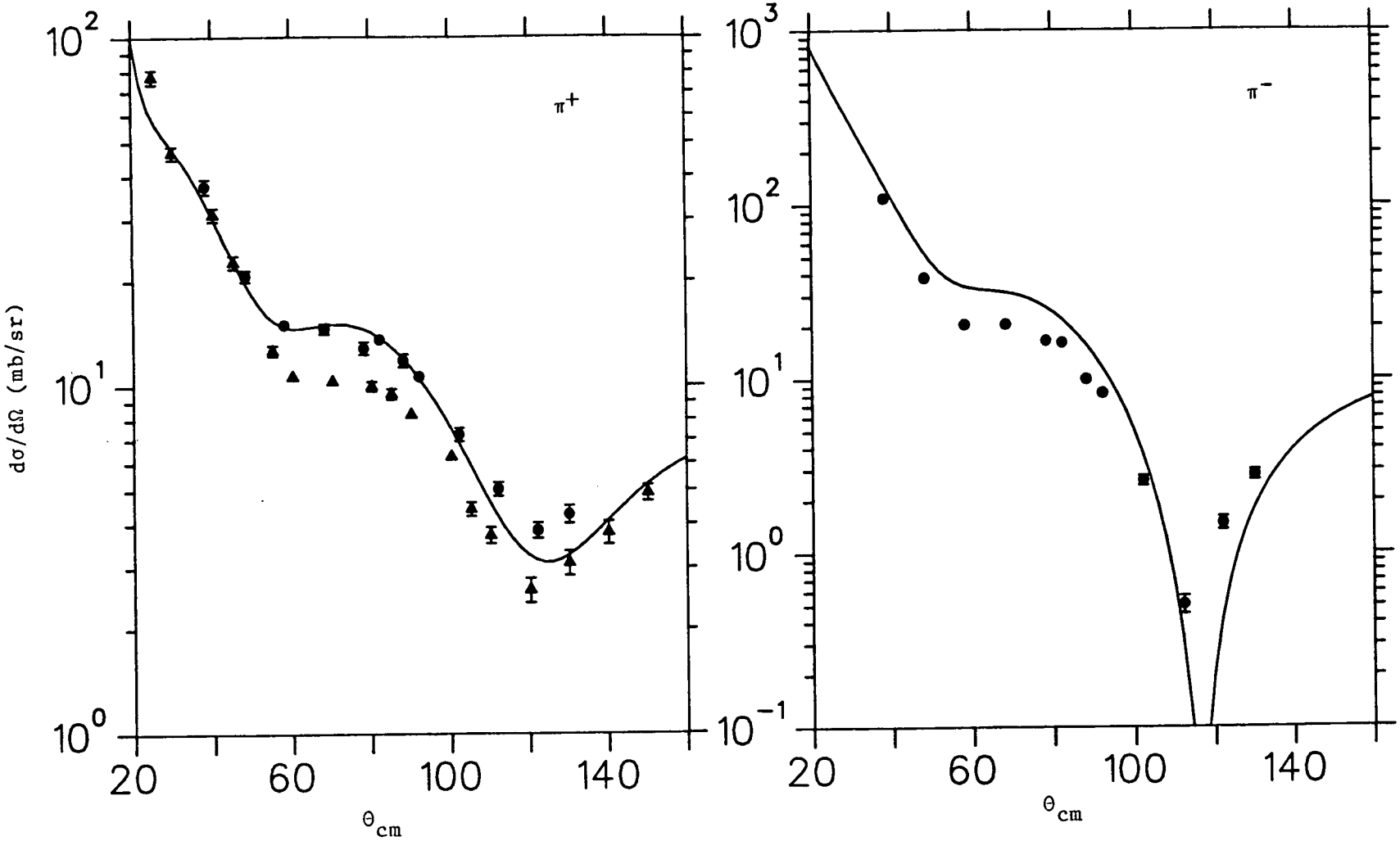

Fig. 5.1 SET E calculations compared to the ^{40}Ca data; ● this experiment, ▲ from (Pre 81)

simultaneously. Different combinations of parameters were allowed to vary from SET E in attempting to fit the data. It became clear that to obtain a good fit, the LLEE parameter, λ, had to be one of the parameters varied. One of the effects of fitting λ (it increases in the fits) is to "soften" the edge of the potential so as to fill in the diffraction minima. The two best fits obtained are shown in Table 5.2, which have three parameters different from SET E. If more than three parameters are free, it becomes increasingly difficult to find a unique minimum in the parameter space due to correlations in the parameters.

The results of FIT B and FIT C are shown in Fig. 5.2 for ^{40}Ca. Each fit has certain points of weakness. FIT C fails to fit the Coulomb-nuclear interference region in the π^+ data, while FIT B does not reproduce the diffractive minimum as effectively. The large value of λ for FIT C is somewhat distasteful (Jen 85) as it is a large departure from the SET E value. This, as well as the slightly better χ^2/ν tends to favor FIT B as the better potential

The absolute cross-section data for ^{48}Ca was not extensively analyzed for determining rms radii differences. This is left to the ratio analysis. To demonstrate that the potentials generated in fitting the ^{40}Ca data reasonably describe the data, the angular distributions generated are shown in Fig. 5.3. The density parameters used are given in Table 5.1 and the resulting χ^2/ν are in Table 5.2. The 68° π^+ ^{48}Ca point looks a bit questionable although no analysis error has been uncovered to date. As the π^+ ^{48}Ca data is not extensively analyzed here, there is no cause for concern on this one data point.

Parameter	FIT B	FIT C
Re b_0	-.0714	
Im c_0	.1003	.0635
Re C_0		1.552
λ	1.836	2.656
$\frac{\chi^2}{\nu}$	^{40}Ca 7.2 ^{48}Ca 7.6	^{40}Ca 7.9 ^{48}Ca 6.8

Table 5.2 The two best potential fits to the absolute ^{40}Ca differential cross-section angular distributions. The potential parameters that are not shown in the table remain at SET E values.

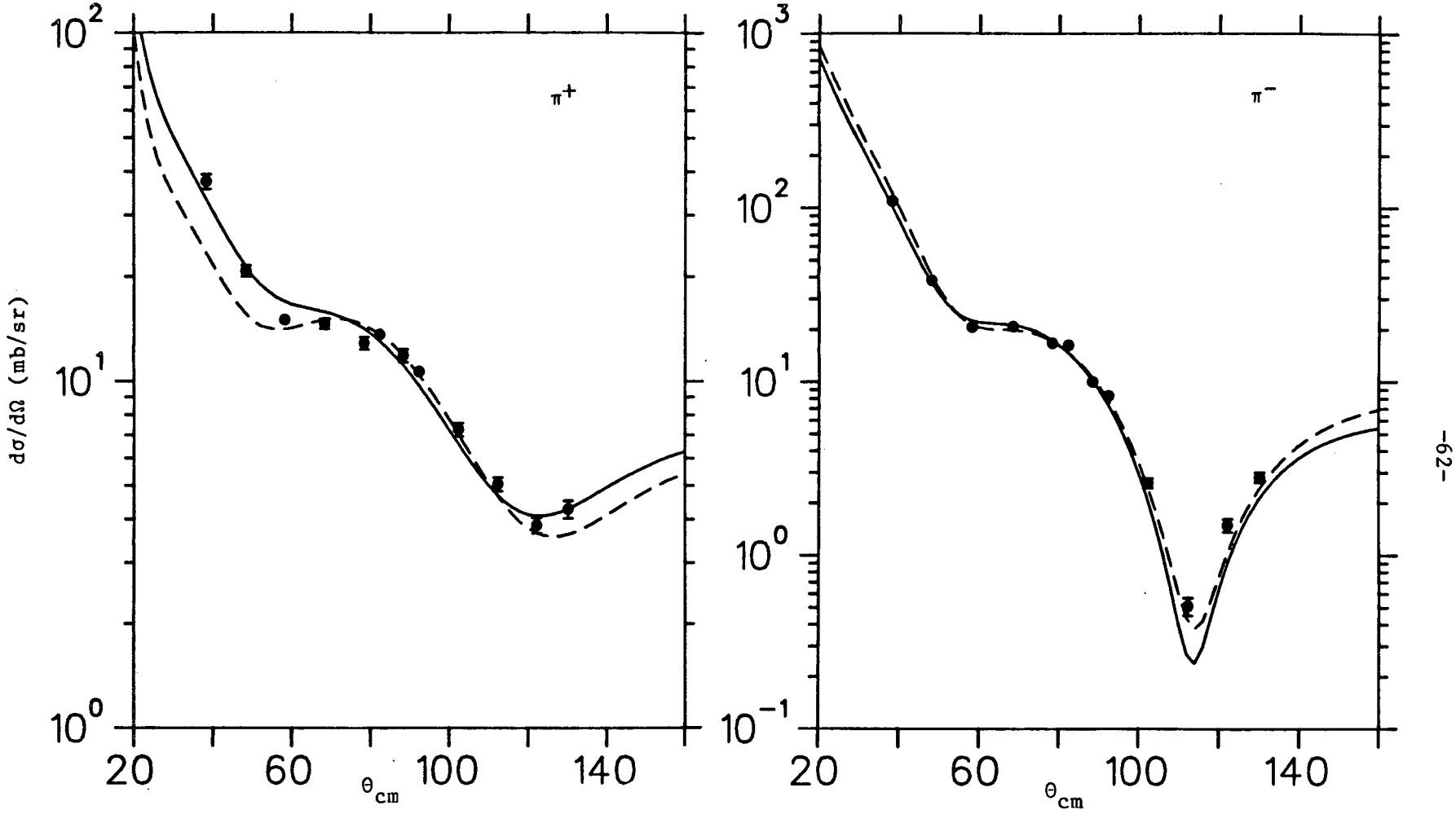

Fig. 5.2 FIT B (solid line) and FIT C (dashed line) potential fits to the ^{40}Ca data.

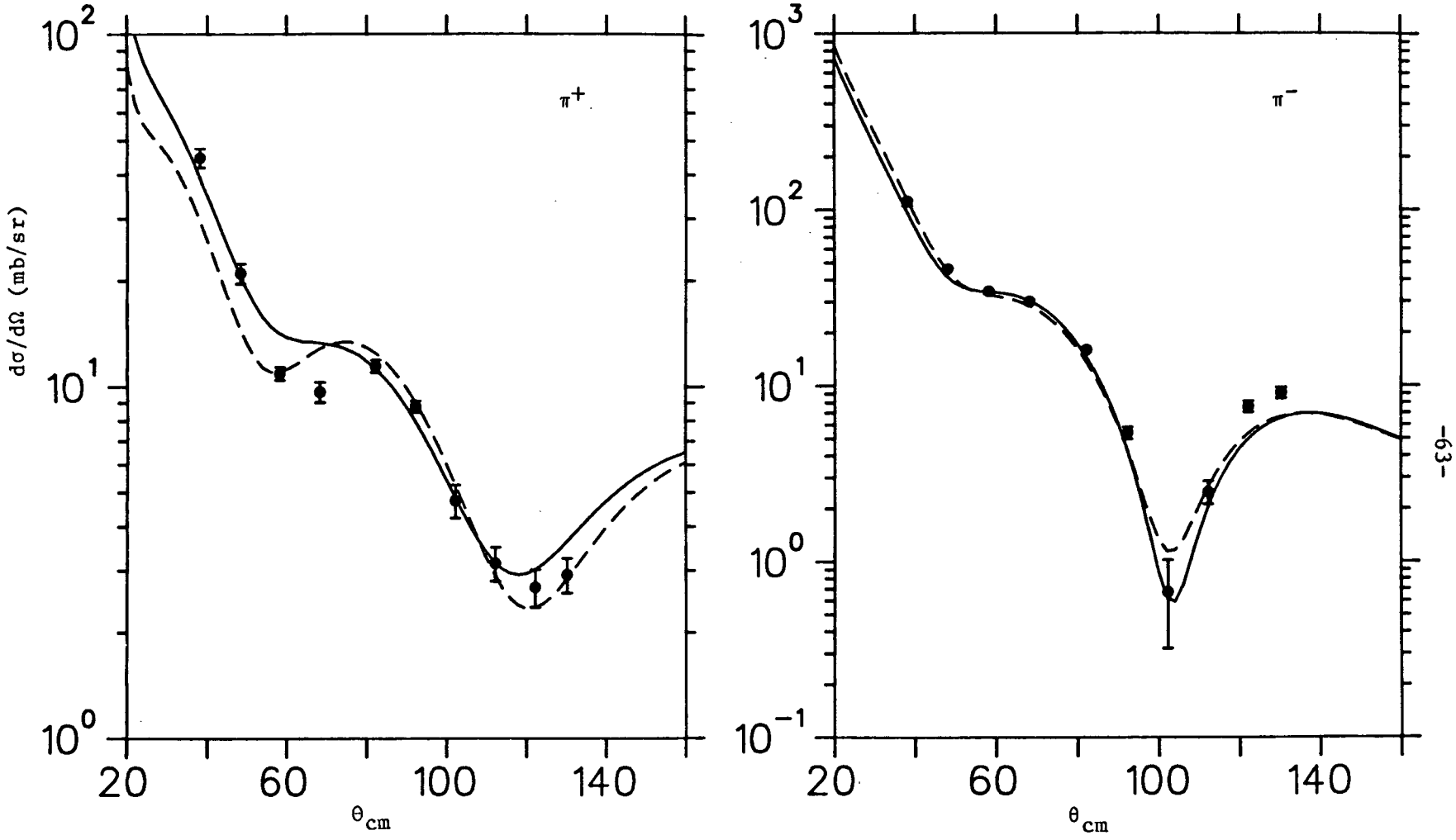

Fig. 5.3 FIT B (solid line) and FIT C (dashed line) potential fits to the ^{48}Ca data.

5.2 Cross-Section Ratio Fitting

The advantage of fitting ratio data versus absolute cross-sections is that many of the systematic errors inherent in the absolute cross-sections will cancel out or at least be substantially reduced in importance. Essentially, only statistical errors in the peak areas contribute to the uncertainty in the ratio. Thus, the determination of $\Delta_{nn'}$ and the density distribution difference, $\Delta\rho_n$, should be obtained more reliably than by fitting to the absolute cross-sections. The ratio data is fitted by varying the shape of the ^{48}Ca neutron distribution, either by changing the parameters of the Fermi distribution (section 5.2.1) or by adding a series of orthogonal polynomials to a starting neutron density to obtain some degree of model independency (section 5.2.2).

5.2.1 Fermi Function Analysis

In the calculation of the rms radius, $\rho(r)$ is weighted by a factor of r^4 (versus a factor of r^2 for the integrated charge). The density near the surface of the nucleus should then be well determined as most of the contribution to the rms radius comes from this part of the nucleus. It is reasonable to expect that if the Fermi density parameters fit the cross-section ratios, the resulting rms radii difference should be valid. This statement is supported by the results of (Gyl 84). The rms radius of the larger isotope obtained from this type of fit will be less reliable than the rms radii difference, being quite dependent upon the parameters assumed for the starting densities not being fitted.

The sensitivity of the extracted rms radii difference to the inclusion of the data in the diffractive region can be checked by fitting

only those data points at less than 95°. The same potentials that are used to fit the whole angular range, that is, FIT B and FIT C, are used to fit the reduced data set. The results of fitting to the whole angular range as well as the reduced range are given in Table 5.3. The results are not statistically independent (they all use data from the same data set), so that an overall average should not be found by treating them as statistically independent. Instead, to reasonably represent the results, taking an unweighted average of the rms radii differences produced by the various fits with an error large enough to encompass all the values produced, we have

$$\Delta_{nn'} = .222 \pm .048 \quad \text{fm.}$$

The error quoted here does not include an estimate of an error contributed due to absolute normalization uncertainties as was done in (Gyl 84) where an estimated contribution of ±.013 fm was taken. The results in Table 5.3 show that there is enough small angle data to obtain a radii difference with errors comparable to the results from the full data set for the Fermi density form. The ratios produced by these fits are shown in Fig 5.4.

Fitting only those data at < 95° produces values of $\Delta_{nn'}$ that are about 40 mfm less than the results from fitting the whole angular range for the same potential, and there is a 55 mfm radii difference between the results from the two potentials. The differences between radii obtained from the reduced data set and the whole data set are somewhat larger than one standard deviation as are the differences in radii from the two potentials. This implies that dependence upon the optical potential has not been removed effectively enough and that the sensitivity of the diffractive region is still large in spite of the

Potential	Data Set	$\Delta_{nn'}$ (fm)	$\frac{\chi^2}{\nu}$	Density Parameters
FIT B	full	.217 ± .024	1.75	a
	reduced	.174 ± .028	1.37	b
FIT C	full	.269 ± .038	3.28	c
	reduced	.230 ± .038	2.14	d

Table 5.3 The rms radii differences obtained by fitting Fermi density forms to the π^- ratio data for the "full" angular distribution and "reduced" set of angles as described in the text. The density parameters are:

a: c_n = 3.867 fm, t_n = .552 fm

b: c_n = 3.976 fm, t_n = .492 fm

c: c_n = 4.018 fm, t_n = .529 fm

d: c_n = 4.124 fm, t_n = .468 fm

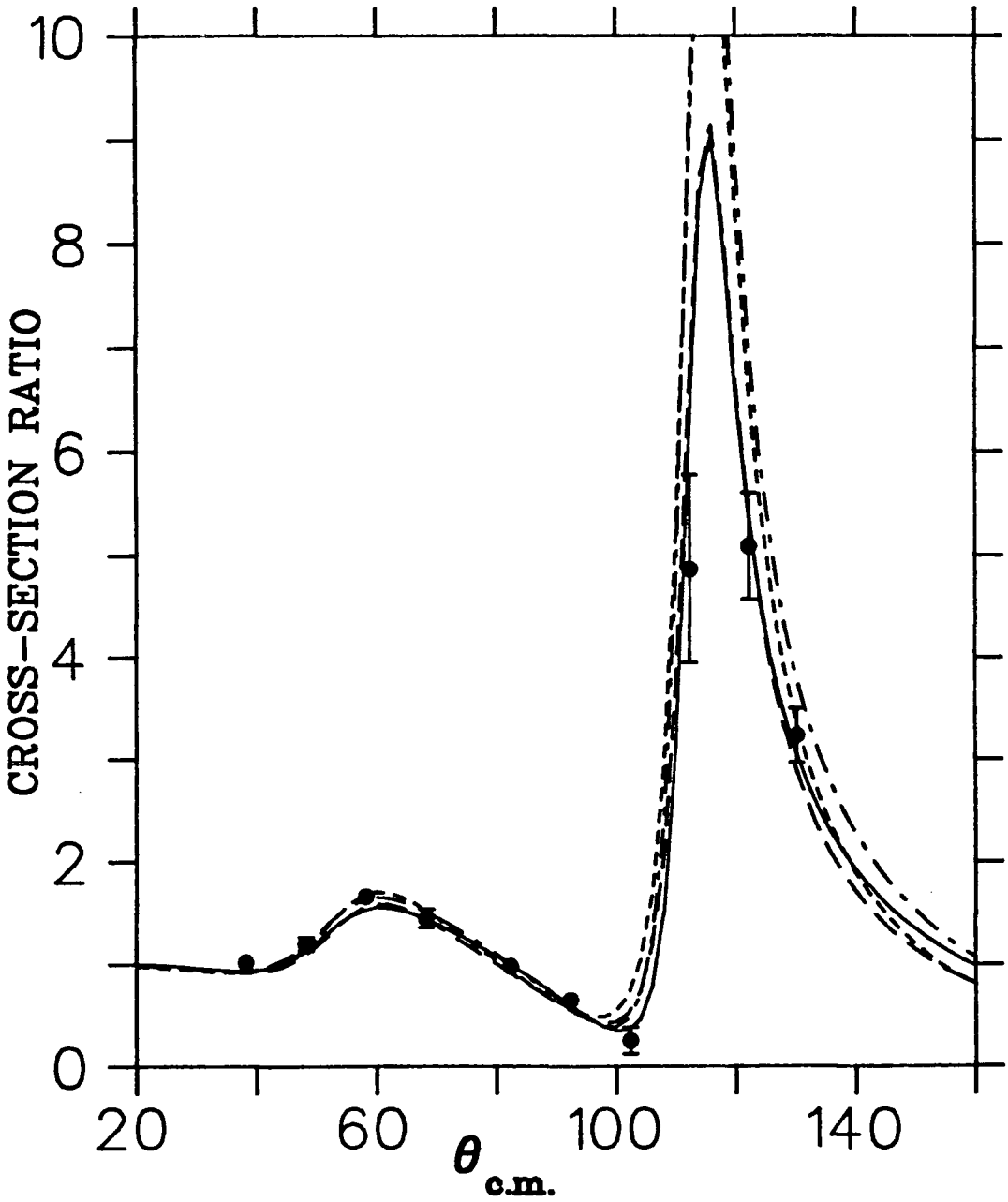

Fig. 5.4 The various Fermi function fits to the ratio data; FIT B full set (solid) and reduced set (dash-dot), FIT C full set (long dash) and reduced set (short dash). The fits are described in the text.

substantial errors in the back angle data. It is important to note that model dependent fits tend to underestimate errors. Realistic errors would improve agreement somewhat, but likely, the errors would not increase enough to markedly reduce the poor agreement. Possible reasons for this lack of agreement will be discussed in section 5.3.

5.2.2 Model Independent Analysis

The 3PF density form used in section 5.2.1 can give accurate descriptions of the rms radii difference that should not have too substantial of an optical model dependence. However, the density distribution difference obtained from these fits would be very dependent upon the exact form taken for the density. The neutron density of ^{48}Ca can be described in a model independent form by adding a series of orthogonal polynomials to a starting density that approximates the neutron density. A Fourier-Bessel expansion can be used as the orthogonal series such that the ^{48}Ca neutron density, $^{48}\rho_n(r)$, can be written as

$$^{48}\rho_n(r) = {}^{48}\rho_F(r) + \sum_n \alpha_n \frac{\sin(\lambda_n r)}{r} \equiv {}^{48}\rho_F(r) + \rho_{FB}(r)$$

where

$$\lambda_n = \frac{n\pi}{R_c}$$

with R_c being the cutoff radius beyond which the Fourier-Bessel contribution is set to zero, and the α_n are the fitted coefficients. $^{48}\rho_F$ is normalized to the number of neutrons in ^{48}Ca. ρ_{FB} is then constrained to have no net contribution to the neutron number. The model independent analysis used the codes implemented by Gyles and Barnett for their thesis work. Further details concerning the analysis techniques can be found in those theses ((Gyl 84, Bar 85)).

The starting density for $^{48}\rho_F$ was taken to be either the best fit parameters in Table 5.3 or it was set such that $(c,t,w)_n = (c,t,w)_p$. If the procedure is truly model independent enough, the starting density used should not affect the final result.

If too many fourier terms are fit to the ratio data, the resulting density distribution difference can oscillate rapidly with radius and tends to have very large errors as a result of correlations in the fourier parameters. Due to the limited momentum transfer available in the data, such oscillations can not be realistically resolved by the pion. If the fourier series is truncated too early, then the polynomials do not have enough freedom to fit any arbitrary density form. That is, a short series is not completely model independent.

It was found to be impossible to obtain results from the Fourier Bessel approach which had at the same time reasonable errors and no fine radial structure in the density distribution difference when fitting the entire angular range of the data. If only the reduced angular data set was fitted, the resulting errors were always very large, indicating that there is insufficient low angle data to fit in this manner.

It is possible that, for this data set, the Fourier-Bessel expansion can not attain enough modelling freedom to fit the neutron density. A different set of orthogonal polynomials may be more suited to this data set, a possibility being the Fourier-Laguerre (FL) expansion described in Appendix VIII of (Bar 85). Fitting with this form of expansion encountered many of the same problems as the Fourier Bessel fitting, however two adequate fits were obtained using the FIT C potential. Fitting with the FIT B potential tended to produce large density variations near the center of the nucleus and the results were

discarded.

The results of these fits are summarized in Table 5.4 and the ratio fits are shown in Fig. 5.5. The neutron radii difference extracted from these two fits agree with each other considering the size of the error in the second fit. Taking the result of the fit with three Fourier-Laguerre parameters (the second fit agrees within its errors), we have

$$\Delta_{nn'} = .110 \pm .022 \text{ fm}$$

for the model independent analysis. This is not in agreement with the Fermi function fit. The density distribution difference obtained is shown in Fig. 5.6. The density distribution difference is displayed in the form $4\pi \cdot r^2 \cdot \Delta\rho_n(r)$ so that the plot indicates the amount of extra neutron density as a function of radius. The shape of the density difference obtained is similar to the results of (Ray 81) except that the maximum in the difference distribution in shifted more to the nuclear interior. This shift is reflected in the smaller rms radii difference obtained in this model independent analysis than that obtained by (Ray 81) (see Table 1.1).

5.3 Discussion

From the discussion of the density analyses above, several points can be made about that calcium data: a) the neutron radii differences obtained have been shown to not be free of model dependency in the description of the neutron density, b) the sensitivity of the ratio data in the diffractive region to the optical parameters cannot be ignored, and c) the model independence that was demonstrated for analysis of data for the sulpher and magnesium isotopes (Gyl 84) has not carried over into

Potential	Number of FL terms	$\Delta_{nn'}$ (fm)	$\frac{\chi^2}{\nu}$
FIT C	3	.110 ± .022	1.68
	5	.081 ± .054	2.38

Table 5.4 The results of the Fourier Laguerre (FL) model independent fits to the ratio data using the FIT C potential. The Fermi part of the density is described by the MIA parameters in Table 5.1.

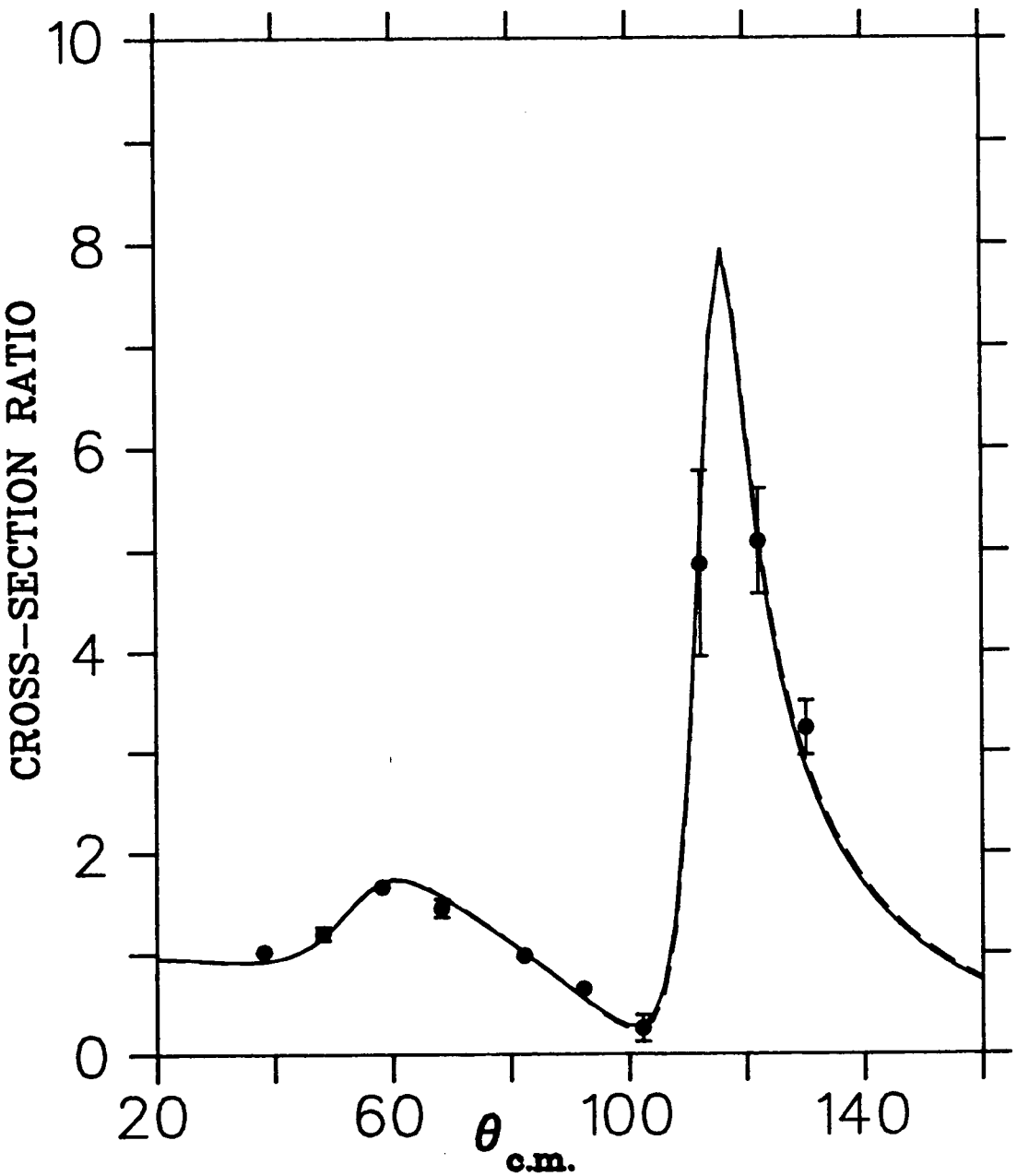

Fig. 5.5 The Fourier-Laguerre fits to the ratio data; three FL parameters (solid), five FL parameters (dashed).

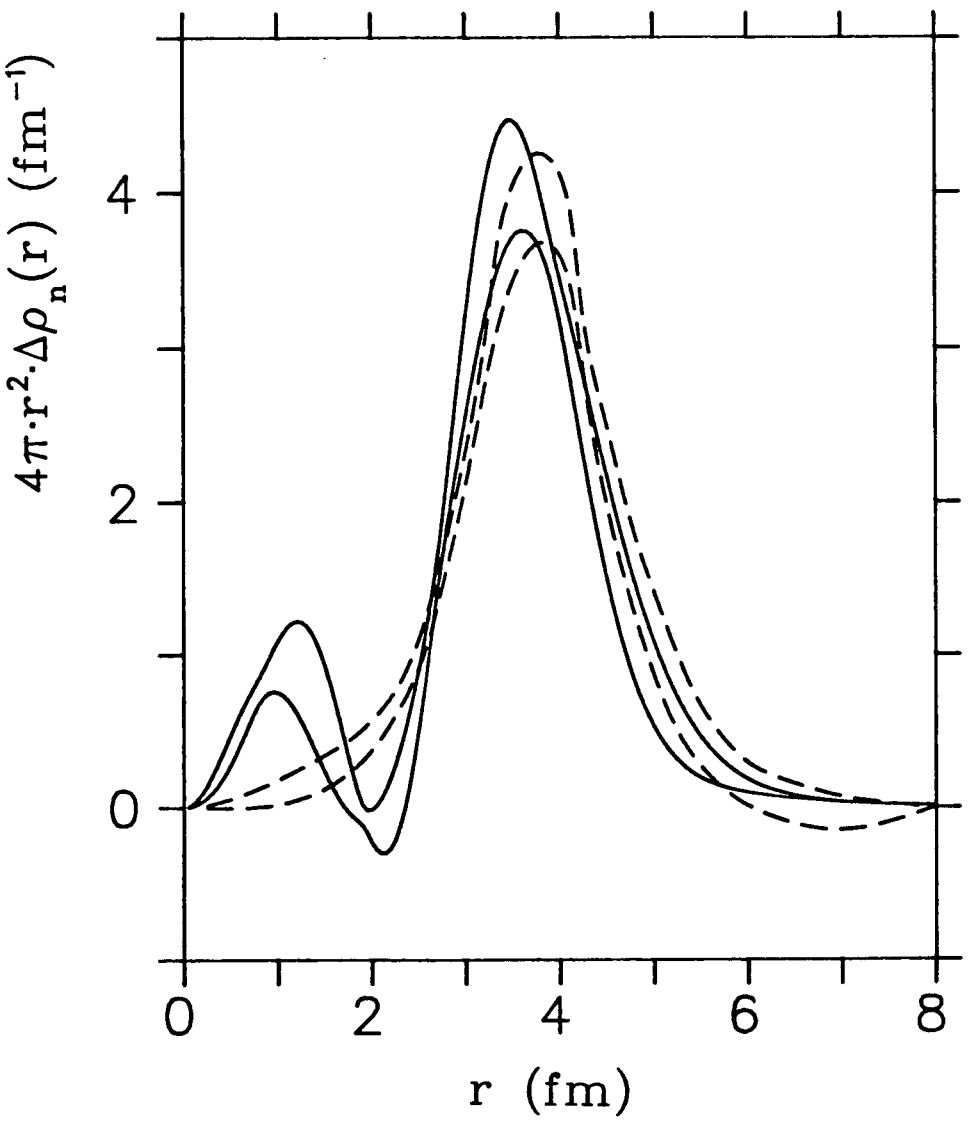

Fig. 5.6 The density distribution difference produced by the Fourier-Laguerre fit (solid) compared to the proton analysis (dashed) of (Ray 81). The lines indicate the upper and lower error bounds obtained in the analysis.

the calcium data.

The difference in atomic number, A, between the two isotopes studied in this experiment is larger than in the isotope (and isotone) pairs previously measured by group members using similar analysis techniques. It is possible that the potential fitted to describe the ^{40}Ca angular distribution does not adequately describe the ^{48}Ca data. That is, even though the χ^2/ν for the ^{48}Ca fits are comparable to the fits to the ^{40}Ca data, the potential may not follow trends developing in the ^{48}Ca angular distribution shape well enough, so that any short comings in the potential are forcibly absorbed into the neutron density of ^{48}Ca. This might distort the shape of the resulting fitted neutron distribution. The difficulties created by taking two nuclei so far apart in A could be reduced by doing an experiment including ^{44}Ca and then analyze the ratios $^{44}\sigma/^{40}\sigma$, $^{48}\sigma/^{44}\sigma$, and $^{48}\sigma/^{40}\sigma$ to try to obtain consistency.To reduce the ratio's sensitivity to the optical potential in the diffractive region, more data would be needed below the minima than was taken for this data set.

The difficulties in fitting the optical potential to the data could also indicate that the form of the potential itself is not adequate. With a reasonable amount of π^- data now available, it is possible that a new global optical potential parameter set with the inclusion of terms that had up to this point been ignored (B_1, C_1, V_c^2, and V_cV_n terms) could be generated to fit both the π^+ and π^- data. Agreement between overlapping data sets from different labs, or sometimes even from the same lab, is not always good (for example, this π^+ ^{40}Ca data and that of (Pre 81)), so that some choice of relative normalization would have to be made, otherwise attempts to improve the optical potential would be limited.

The consistency of the analysis method used for the π^- ratio data could be checked by analyzing the π^+ ratios. The ratio difference obtained should be consistent with values from the precision electron and muon experiments. This has not yet been done for this data, but the model independent methods have been applied to π^+ scattering (see especially (Bar 85)) where consistency has been demonstrated.

The results obtained for the radii difference, $\Delta_{nn'}$, are

$$\Delta_{nn'} = .222 \pm .048 \text{ fm}$$

for the Fermi function fit, and

$$\Delta_{nn'} = .110 \pm .022 \text{ fm}$$

for the Fourier-Laguerre fitting. The results do not agree well. Some possible causes for this discrepancy have been suggested above. For incompressible nuclear matter, the radius should follow an $A^{1/3}$ trend so that the rms radii difference would be

$$\delta r = \Delta_{nn'} = \frac{r}{3} \frac{\delta A}{A} .$$

This model gives

$$\Delta_{nn'} = .227 \text{ fm}$$

which agrees well with the Fermi function fit result.

The $\Delta_{nn'}$ from the Fermi fit is more more consistent with the most recent model independent analyses of proton (Ray 81) and α (Gil 84) scattering than is the result from the Fourier-Laguerre fitting (see Table 1.1). However, as the analysis of this calcium data set has not been demonstrated to be free of dependence upon the density form chosen for the ^{48}Ca neutron distribution, nor to be free of the diffractive

sensitivity in the optical potential, a conclusive comparison is not yet warranted. Further analysis may solve some of these difficulties. However, it appears, at present, that the calcium isotopes (and other nuclei in the $f_{7/2}$ shell) are just slightly too large in atomic number for elastic pion scattering at 50 MeV to be analyzed in a model independent fashion through the methods developed and used in (Gyl 84, Bar 85).

REFERENCES

Arn 82 R.A. Arndt and L.D. Roper, SAID: Scattering Analysis and Interactive Dialin Program, Center for Analysis of Particle Scattering, Virginia Polytechnic Institute and State University Internal Report CAPS-80-3 (1982).

Bar 85 B.M. Barnett, Ph. D. Thesis, Univ. of British Columbia, unpublished, (1985).

Bat 69 C.J. Batty and G.W. Greenless, Nucl. Phys. A133 (1969) 673.

Ber 72 W. Bertozzi, J. Friar, J. Heisenberg and J.W. Negele, Phys. Lett. 41B (1972) 408.

Car 82 J.A. Carr, H. McManus and K. Stricker-Bauer, Phys. Rev. C25 (1982) 952.

Cha 78 A. Chameaux, V. Layly and R. Schaeffer, Ann. Phys. 116 (1978) 247.

Daw 81 G.H. Daw, M. Sc. Thesis, New Mexico State Univ., unpublished (1981).

Eis 76 R.A. Eisenstein and G.A. Miller, Comp. Phys. Comm. 11 (1976) 95.

Eis 80 J.M. Eisenberg and D.S. Koltun, Theory of Meson Interactions with Nuclei, Wiley (1980).

Eri 66 M. Ericson and T.E.O. Ericson, Ann. Phys. 36 (1966) 323.

Fri 79 J. Friedrich, contribution to (Reb 79).

Fro 68 R.F. Frosch, R. Hofstadter, J.S. McCarthy, G.K. Noldeke, K.J. Van Oostrum, B.C. Clark, R.Herman and D.G. Ravenhall, Phys. Rev. 174 (1968) 1380.

Gil 84 H.J. Gils, H. Rebel and E. Friedman, Phys. Rev. C28 (1984) 1295.

Gyl 84 W. Gyles, Ph. D. Thesis, Univ. of British Columbia, unpublished (1984), and W. Gyles, B.M. Barnett, R. Tacik, K.L. Erdman, R.R. Johnson, G.J. Lolos, H. Roser, K.A. Aniol, F. Entezami, E.L. Mathie, D.R. Gill, E.W. Blackmore, C.A. Wiedner, S. Martin, R.J. Sobie, and T.E. Drake, Nucl. Phys. A439 (1985) 598.

Hes 85 N.P. Hessey, M. Sc. Thesis, Univ. of British Columbia, unpublished, (1985).

Jak 77 M.J. Jakobson, G.R. Burleson, J.R. Calarco, M.D. Cooper, D.C. Hagerman, I. Halpern, R.H. Jeppeson, K.F. Johnson, L.D. Knutson, R.E. Marrs, H.O. Meyer and R.P. Redwine, Phys. Rev. Lett. 38 (1977) 1201.

Jen 85 B. Jennings, private communication.

Ker 59 A.K. Kerman, H. McManus and R.M. Thaler, Ann. Phys. 8 (1951) 551.

Kre 68 M. Krell and T.E.O. Ericson, J. Comp. Phys. 3 (1968) 202.

Lat 47 C.M.G. Lattes, H. Muirhead, C.F. Powell and G.P. Occhialini, Nature 159 (1947) 694.

Neg 70 J.W. Negele, Phys. Rev. C1 (1970) 1260.

Neg 72 J.W. Negele and D. Vautherin, Phys. Rev. C5 (1972) 1472.

Nol 69 J.A. Nolan and J.P. Schiffer, Ann. Rev. Nucl. Sci. 19 (1969) 475.

Ora 81 C.J. Oram, J.B. Warren, G. Marshall and J. Doornbos, Nucl. Inst. Meth. 179 (1981) 95.

Pow 80 R.J. Powers, K.-C. Wang, M.W. Hoehn, E.B. Shera, E.D. Wohlfahrt and A.R. Kunselman, Nucl. Phys. A336 (1980) 475.

Pre 81 B.M. Preedom, S.H. Dam, C.W. Darden, R.D. Edge, D.J. Malbrough, T. Marks, R.L. Burman, M. Hamm, M.A. Moinester, R.P. Redwine, M.A. Yates, F.E. Bertrand, T.P. Cleary, E.E. Gross, N.W. Hill, C.A. Ludemann, M. Blecher, K. Gotow, D. Jenkins and F. Milder, Phys. Rev. C23 (1981) 1134.

Ray 79 L. Ray, Phys. Rev. C19 (1979) 1855.

Ray 81 L. Ray, G.W. Hoffman, M. Barlett, J. McGill, J. Amann, G. Adams, G. Pauletta, M. Gazzaly and G.S. Blanpied, Phys. Rev. C23 (1981) 828.

Reb 79 "What Do We Know about the Radial Shape of Nuclei in the Ca-Region?", Proceedings of the Karlsruhe International Discussion Meeting, ed. H. Rebel, H.J. Gils and G. Schatz, (1979).

Rut 11 E. Rutherford, Phil. Mag., (1911) 669.

Sin 73 B.B.P. Sinha, G.A. Peterson, R.R. Whitney, I. Sick and J.S. McCarthy, Phys. Rev. C7 (1973) 1930.

Sob 84a R.J. Sobie, Ph. D. Thesis, Univ. of Toronto, unpublished (1984) and R.J. Sobie, T.E. Drake, K.L. Erdman, R.R. Johnson, H.W. Roser, R. Tacik, E.W. Blackmore, D.R. Gill, S. Martin, C.A. Wiedner and T. Masterson, Phys. Rev. C30 (1984) 1612.

Sob 84b R.J. Sobie, T.E. Drake, B.M. Barnett, K.L. Erdman, W. Gyles, R.R. Johnson, H.W. Roser, R. Tacik, E.W. Blackmore, D.R. Gill, S. Martin, C.A. Wiedner and T. Masterson, Nucl. Inst. Meth. 219 (1984) 501.

Str 79 K. Stricker, H. McManus and J.A. Carr, Phys. Rev. C19 (1979) 929.

Str 80 K. Stricker, J.A. Carr and H. McManus, Phys. Rev. C22 (1980) 2043.

Tac 84 R. Tacik, Ph. D. Thesis, Univ. of British Columbia, unpublished (1984).

Thi 76 M. Thies, Phys. Lett. 63B (1976) 43.

Tho 81 A.W. Thomas, Nucl. Phys. 354 (1981) 51c.

Var 77 G.K. Varma and L. Zamick, Phys. Rev. C16 (1977) 308.

Vau 70 D. Vautherin and D.M. Brink, Phys. Lett. 32B (1970) 149.

Vau 72 D. Vautherin and D.M. Brink, Phys. Rev. C5 (1972) 626.

Woh 81 H.D. Wohlfahrt, E.B. Shera, M.V. Hoehn, Y. Yamazaki and R.M. Steffen, Phys. Rev. C23 (1981) 523.

Yuk 35 H. Yukawa, Proc. Physico-Math. Soc. Japan 17 (1935) 48.